Revised Manuscript (Unmarked version)

Transient Hydrodynamic Stresses on Reciprocating Hollow Fibers using Hydro-Rattle Algorithm: A Constraint Dissipative Hydrodynamics Simulation

Albert S. Kim[a,*], Hyeon-Ju Kim[b], Kwang Jin Lee[c], Moo Seok Lee[c]

[a] *Civil and Environmental Engineering, University of Hawaii at Manoa, 2540 Dole Street, Holmes 383, Honolulu, Hawai'i, 96822*
[b] *Offshore Plant and Marine Energy Research Division, Korea Research Institute of Ships and Ocean Engineering, 32 Yuseong-daero 1312 beon-gil, Yuseong-gu, Daejon 34103, Korea*
[c] *Business Division 2, Kolon Industries, Inc., Kolon One&only tower, Magokdong-ro 110, Gangseo-gu, Seoul 07793, Republic of Korea*

Abstract

Hollow fiber membranes are widely used for unit processes in wastewater treatment, including (submerged) membrane bioreactors. Interfacial fouling on the fiber surfaces, often caused by small fiber diameters, is controlled, using energy-intensive bubble blowers. A new cost-effective paradigm is to reciprocate submerged cassettes that carry hollow fibers undergoing hydrodynamic shear stresses. Oscillation dynamics of flexible fibers seems to be a challenging investigation because fluid-fiber hydrodynamic interactions need to be rigorously formulated while applying the wave equation is precluded. As the order-of-magnitude estimation of mechanical stresses on moving fibers is of great interest, we assumed that a hollow fiber can be mathematically modeled as a chain of many connected spheres of an order of $O(10^3)$, having the chain length and sphere diameter set equal to those of identical fibers. Holonomic and non-holonomic constraints are implemented to keep spheres from dispersing and the dissipative hydrodynamics, and to satisfy the position-velocity orthogonality. Hydrodynamic interactions were calculated using the grand-mobility matrix of poly-dispersed spheres, and the constraint forces are implemented using an updated algorithm of Hydro-Rattle [Kim,

*Corresponding author: Tel: 808-956-3718, Fax: 808-956-5014
Email address: albertsk@hawaii.edu (Albert S. Kim)
URL: albertsk.org (Albert S. Kim)

Chemistry Letters, 41(10):1285–1287, 2012]. Dynamic locations of the highest mechanical stresses are identified, and practical suggestions for the optimal, long-term operations of the cassette-reciprocating process are included.

Keywords: Submerged hollow fibers, Low Energy No Aeration process, Chain Dynamics, Hydro-Rattle algorithm, Dissipative Hydrodynamics

---

1. Introduction

For municipal and industrial wastewater treatment, membrane bioreactor (MBR) is widely used as a combined process of membrane separation processes such as microfiltration/or ultrafiltration and biological wastewater treatment [1–6]. As interstitial spaces between packed fibers are of the same order as the fiber thickness [7], membrane fouling due to the accumulation of chemical and biological (solid) materials on fiber surfaces has limited the MBR performance of wastewater treatment. A recent advance of the MBR process includes co-processing with forward osmosis [8], of which flux discrepancy is partially solved by introducing the interfacial porosity [9]. Hollow fiber (HF) membranes are often preferred in many MBR applications due to the high packing ratio from small strand diameter, flexibility of fiber configurations, availability of backwashing [10], and chemical resistance to high total suspended solid concentrations. A standard cleaning or fouling-reduction method is to diffuse small bubbles using blowers from the bottom of the vertically packed membranes [11–15]. However, steady generation and distribution of small, equal-sized bubbles are usually costly.

Theoretical and numerical studies of MBR processes are often challenging, as the processes contains physical, chemical, biological, and fluid dynamic phenomena in a strongly coupled way at multiple length and time scales. HF modeling studies for MBR application include: CFD of aeration influenced by module design [16], energy analysis and optimization of HF MBR for gas-liquid mass transfer and recovery [14, 17], and optimal module configurations for efficient bubble cleaning for HF MBR [18, 19]. The aeration has been widely used to mitigate membrane fouling, by producing small bubbles at the bottom of HF membrane bundles installed in submerged MBR systems. Floating bubbles physically interact with accumulated particulate materials and hinder further deposition on outer HF membrane surfaces. Smaller bubble sizes are required to maximize the efficiency of bubble dynamics, which requires high electricity consumption. Because real-time identification and removal of foulants in MBR processes are often difficult due to unsteady variation of

feed compositions and concentrations, it is fundamentally questionable that instantaneous bubble-size optimization can significantly reduce HF surface fouling to a certain degree while HFs are not rigidly fixed, being submerged in MBR tanks. Unless fibers are well-positioned, vertically moving bubbles may generate preferential bubble-flow between biased interstitial spaces between fibers.

A new mechanism of fouling reduction was recently proposed by the membrane industry, which is to reciprocate the attached HF bundles on cassettes using a motor and crank to generate a wavy, oscillatory motion of hanging fibers in an MBR tank. The relative motion of the cassettes to the fluid generates shear forces on attached foulants and therefore reduces, minimizes, and prevents contact probabilities of suspended solids on membrane surfaces. This new method is called Low Energy No Aeration (LENA) as shown in Fig. 1, which was recently developed by Kolon Industry in South Korea. Counter-intuitively, LENA consumes 25% less energy than MBR systems that use conventional bubble blowers. A potential concern is the mechanical stability of the HFs attached to cassettes in periodic reciprocation dynamics.

Within state-of-the-art computational advances, dynamics of the long, flexible fiber under the viscous flow field is challenging work [20–22]. Although the fiber motion resembles a wavy oscillatory motion (e.g., of a musical instrument like guitar strings), the finite fiber length precludes the wave equation as a governing equation, and mandates sophisticated theoretical and simulational approaches. In this light, we mimic the flexible HF (under periodic motion) as a linear collection of linked spheres, i.e., a particle chain, by incorporating constrained dynamics under dissipative hydrodynamics [23]. Forces exerted on small local segments of a HF, including gravitational, hydrodynamic, and constraint forces, are calculated as those acting on a sphere whose diameter is equal to that of the fibers' outer diameter. Based on the simulation results of force calculations, several suggestions for HF manufacturing and operating cassette reciprocating are provided.

2. Theory and Simulation

A single HF motion of reciprocation is modeled, using the algorithm developed in this section. Two necessary conditions for a fiber to be met are the mechanical flexibility and the finite length: the former precludes using the wave equation, and the latter initiates the equivalency between a flexible fiber and a particle chain.

2.1. Constrained Dynamics

Constrained molecular dynamics has been widely used to model rigid bodies of non-spherical shapes, which include bonded and compound molecules. In general, constraint equations are determined, such as center-to-center distance or their torsion angles between two volumeless molecules. Because these constraints should be satisfied at any time t, they are included in the potential function of the entire particulate system. The spatial derivative provides the constraint forces. These constraint forces include unknown parameters, called Lagrange multipliers, which are calculated instantaneously at time t to maintain the chain connectability. A vector sum of the external and constraint (internal) forces allow the non-spherical rigid bodies to move, keeping their geometrical configurations. Two representative algorithms to solve the constrained dynamics problems are SHAKE [24] and RATTLE [25]. As the review of constrained dynamics is out of our research scope, we discuss only the theoretical aspect of how the RATTLE algorithm is combined with the standard dissipative hydrodynamics [23, 26], including some detailed advances of this work.

2.2. Forces

2.2.1. Constraint forces

A HF membrane of length l_f and diameter d_f is modeled as a chain of N_p spheres of the same diameter. Sphere k is characterized using its radius $a_k = \frac{1}{2}d_f$, volume $\frac{4\pi}{3}a_k^3$, and mass $m_k \left(= \frac{4\pi}{3}a_k^3\rho_k\right)$, where ρ_k is the solid mass density of the sphere. During the motion of the chain, center-to-center distance between sphere k and $k+1$, denoted $d_{k,k+1}$, for $k = 1$ to

$N_p - 1$ is maintained invariant at any time t:

$$\sigma_k = (\boldsymbol{r}_k - \boldsymbol{r}_{k+1})^2 - d_{k,k+1}^2 = 0 \tag{1}$$

$$d_{k,k+1} = a_k + a_{k+1} + d_s \tag{2}$$

where d_s is the surface-to-surface distance between the two neighboring spheres, often set zero. Because the HF has a uniform thickness, spheres are considered as mono-dispersed, i.e., $a_k = a_{k+1} = a_f = \frac{1}{2}d_f$, having constant mass density of $\rho_k = \rho_p$. Sphere k connected to $k+1$ and $k-1$ in the chain is shown in Fig. 2.

In the motion of connected spheres, sphere k experiences the external (i.e., unconstrained) as well as the constraint forces simultaneously. The external forces include the conservative gravitational force and the dissipative hydrodynamic interactions. The constraint forces are instantaneously generated, as responses to all unconstrained forces, to satisfy $N_p - 1$ geometrical conditions of Eq. (1). To investigate the dynamic phenomena of the long chain, we improved the hydro-rattle algorithm [23] and performed the many-body constrained dissipative hydrodynamics (CDHD) simulations.

First of all, the unconstrained and constraint forces are described as

$$\boldsymbol{f}_k^* = m_k \boldsymbol{a}_k^* \tag{3}$$

and

$$\boldsymbol{f}_k^c = m_k \boldsymbol{a}_k^c = -\nabla_k \Phi^c \tag{4}$$

respectively, where $\boldsymbol{a}_k^*$ and $\boldsymbol{a}_k^c$ are unconstrained and constraint accelerations of particle k, respectively. The constraint force of Eq. (4) is obtained using a potential function, defined as

$$\Phi^c = \frac{1}{2}\sum_{k=1}^{N_p-1} \lambda_k \sigma_k \tag{5}$$

where the coefficient $\frac{1}{2}$ is included by convention and λ_k is the Lagrange multiplier that will

be instantaneously calculated at time t. Using the definition of $\boldsymbol{f}_k^c = -\nabla_k \Phi^c$, one calculates the constraint force exerted on sphere k, connected to sphere $k-1$ and $k+1$, as

$$m_k \boldsymbol{a}_k^c = \lambda_{k-1} \left(\boldsymbol{r}_{k-1} - \boldsymbol{r}_k \right) - \lambda_k \left(\boldsymbol{r}_k - \boldsymbol{r}_{k+1} \right) \tag{6}$$

where the Lagrange multipliers λ_{k-1} and λ_k for sphere k are determined to maintain the sphere connectability. Because the total acceleration of sphere k is a vector-wise superposition of unconstrained and constraint accelerations, i.e., $\boldsymbol{a}_k = \boldsymbol{a}_k^* + \boldsymbol{a}_k^c$, the velocity of sphere k evolves from $\boldsymbol{v}_k(t)$ to that of the next time step $t^+ = t + h$ with a time interval h in two steps:

$$\boldsymbol{v}_k^* \left(t^+ \right) = \boldsymbol{v}_k(t) + h \boldsymbol{a}_k^* \tag{7}$$

$$\boldsymbol{v}_k \left(t^+ \right) = \boldsymbol{v}_k^* \left(t^+ \right) + h \boldsymbol{a}_k^c \tag{8}$$

where $\boldsymbol{v}_k^*(t^+)$ is the unconstrained evolution of the velocity from time t to $t+h$. Sphere k of velocity $\boldsymbol{v}_k$ at time t will have a new velocity $\boldsymbol{v}_k^*(t^+)$ after time h, driven by the unconstrained acceleration $\boldsymbol{a}_k^*$ and will secondarily evolve to $\boldsymbol{v}_k(t^+)$ by the holonomic constraint acceleration $\boldsymbol{a}_k^c$. Similarly, the position of sphere k, $\boldsymbol{r}_k(t)$, changes from time t to t^+:

$$\boldsymbol{r}_{ik}^* \left(t^+ \right) = \boldsymbol{r}_k(t) + h\, \boldsymbol{v}_k(t) + \tfrac{1}{2} h^2 \boldsymbol{a}_k^* \tag{9}$$

$$\boldsymbol{r}_k \left(t^+ \right) = \boldsymbol{r}_k^* \left(t^+ \right) + \tfrac{1}{2} h^2 \boldsymbol{a}_k^c \tag{10}$$

where $\boldsymbol{r}_i^*(t^+)$ is the unconstrained evolution of $\boldsymbol{r}_i(t)$. Eqs. (7) and (9) mathematically imply the sequential time-evolution of the velocity and position, respectively, by the unconstrained forces first and constraint forces later. After the time evolution under the net forces, the constraint Eq. (1) should be satisfied for sphere k such that

$$\left[\Delta \boldsymbol{r}_{k,k+1}^+ \right]^2 - d_{k,k+1}^2 = 0 \tag{11}$$

where

$$\Delta \boldsymbol{r}^{+}_{k,k+1} = \boldsymbol{r}_k\left(t^+\right) - \boldsymbol{r}_{k+1}\left(t^+\right) = \Delta \boldsymbol{r}^{*}_{k,k+1} + \tfrac{h^2}{2}\,\Delta \boldsymbol{a}^{c}_{k,k+1} \tag{12}$$

is the relative position of sphere k with respect to $k+1$, and

$$\Delta \boldsymbol{a}^{c}_{k,k+1} = \lambda_{k-1} m_k^{-1} \Delta \boldsymbol{r}_{k-1,k} + \lambda_k m_{k+1}^{-1} \Delta \boldsymbol{r}_{k,k+1} - \lambda_k \mu_{k,k+1}^{-1} \Delta \boldsymbol{r}_{k,k+1} \tag{13}$$

is the relative constraint acceleration of sphere k, where $\mu_{k,k+1} = \left(m_k^{-1} + m_{k+1}^{-1}\right)^{-1}$ is the reduced mass. Substitution of Eqs. (12) and (13) in (11) gives

$$\lambda_k h^2 = \frac{\left(\Delta \boldsymbol{r}'_{k,k+1}\right)^2 - d^2_{k,k+1} + \frac{\lambda_k^2 h^2}{4\mu_{k,k+1}} \left(\Delta \boldsymbol{r}_{k,k+1}\right)^2}{\mu^{-1}_{k,k+1} \Delta \boldsymbol{r}'_{k,k+1} \cdot \Delta \boldsymbol{b}_{k,k+1}} \tag{14}$$

where

$$\Delta \boldsymbol{r}'_{k,k+1} = \Delta \boldsymbol{r}^{*}_{k,k+1}\left(t^+\right) + \tfrac{h^2}{2} m_k^{-1} \lambda_{k-1} \Delta \boldsymbol{r}_{k-1,k}\left(t\right) + \tfrac{h^2}{2} m_{k+1}^{-1} \lambda_{k+1} \Delta \boldsymbol{r}_{k+1,k+2}\left(t\right) \tag{15}$$

indicates the unconstrained position evolution of $\Delta \boldsymbol{r}^{*}_{k,k+1}$ and constrained evolution represented using the Lagrange multipliers. Eq. (14) is quadratic for λ_k, which uses unknown values of λ_{k-1} and λ_{k+1} at time t. Instead of solving a linear system of tridiagonal matrix of λ_k, one can use initially guessed or well-educated values of λ_{k-1}, λ_k, and λ_{k+1} to evaluate the right-hand side of Eq.(14) and update λ_k on the left-hand side. While λ_k is iteratively updated until it converges to a constant value within a tolerable error, λ_{k-1} and λ_{k+1} are maintained fixed. A simpler version of Eq. (14) is one that was previously used [23]:

$$\lambda_k h^2 \simeq \frac{\left(\Delta \boldsymbol{r}^{*}_{k,k+1}\right)^2 - d^2_{k,k+1}}{\mu^{-1}_{k,k+1} \Delta \boldsymbol{r}^{*}_{k,k+1} \cdot \Delta \boldsymbol{b}_{k,k+1}} \tag{16}$$

that neglected higher order terms of h^2 in Eq. (14). Eq. (16) is straightforward to numerically update λ_k from time stem t to t^+, but neglecting the higher order terms may slow down the

iteration processes, and therefore cause lower converging efficiency.

After positions of all the spheres are found at time t^+ under the influence of both the constraint and unconstrained forces, the linear velocities need to be corrected by the orthogonality condition:

$$(\boldsymbol{r}_j - \boldsymbol{r}_{j+1}) \cdot (\boldsymbol{v}_j - \boldsymbol{v}_{j+1}) = 0 \tag{17}$$

which is obtained by differentiating holonomic constraint Eq. (1) with respect to time. The evolution of velocity is calculated as

$$\boldsymbol{v}_j\left(t^+\right) = \tilde{\boldsymbol{v}}_j\left(t^+\right) + h\boldsymbol{a}_j^n \tag{18}$$

$$\tilde{\boldsymbol{v}}_j\left(t^+\right) = \boldsymbol{v}_j\left(t\right) + h\left(\boldsymbol{a}_j^* + \boldsymbol{a}_j^c\left(t\right)\right) \tag{19}$$

after the holonomically constrained evolution of position and velocity of Eqs. (7)-(10), which satisfies Eq. (1) at an arbitrary time t. In other words, sphere j is accelerated externally by $\boldsymbol{a}_j^*$ of Eq. (7), holonomically by $\boldsymbol{a}_j^c$ of Eq.(8), and then non-holonomically by $\boldsymbol{a}_j^n$ of Eq. (18). In this section, we used sphere indices k and j to distinctly discuss the holonomic and non-holonomic constraints, respectively, without implementing any new physical aspect. Although the constraint forces satisfy the holonomic constraint, it does not guarantee that the orthogonality condition is also met. Therefore, similar to the constraint acceleration $\boldsymbol{a}_k^c$, the non-holonomic acceleration $\boldsymbol{a}_j^n$ is originated from Eq. (17):

$$\boldsymbol{a}_j^n = \kappa_{j-1}\left(\boldsymbol{r}_{j-1} - \boldsymbol{r}_j\right) - \kappa_j\left(\boldsymbol{r}_j - \boldsymbol{r}_{j+1}\right) \tag{20}$$

and furthermore,

$$\Delta\boldsymbol{a}_{j,j+1}^n = m_j^{-1}\Delta\boldsymbol{r}_{j-1,j}\kappa_{j-1} + m_{j+1}^{-1}\Delta\boldsymbol{r}_{j,,j+1}\kappa_{j+1} - \left(m_j^{-1} + m_{j+1}^{-1}\right)\Delta\boldsymbol{r}_{j,,j+1}\kappa_j \tag{21}$$

where $\boldsymbol{\kappa}$ is a new Lagrange multiplier to satisfy the orthogonality Eq. (17), indicating that the scalar product of relative position and relative velocity between two adjacent spheres is

always zero. Then, we calculate the relative velocity of sphere j with respect to $j+1$ that satisfy Eqs. (1) and (17) as

$$\Delta \boldsymbol{v}_{j,j+1}\left(t^{+}\right) = \Delta \boldsymbol{v}'_{j,j+1} - \tfrac{h^2}{2}\kappa_j \mu^{-1}_{j,j+1}\Delta \boldsymbol{r}_{j,j+1} \tag{22}$$

where

$$\Delta \boldsymbol{v}'_{j,j+1} = \Delta \boldsymbol{v}^{*}_{j,j+1} + \tfrac{h^2}{2} m_j^{-1}\Delta \boldsymbol{r}_{j-1,j}\kappa_{j-1} + \tfrac{h^2}{2} m_{j+1}^{-1}\Delta \boldsymbol{r}_{j,,j+1}\kappa_{j+1} \tag{23}$$

is the relative velocity under the influences of unconstrained evolution and orthogonal constraints with the two touching neighbors. Using the similar approach to obtain λ_k of Eq. (14), one derives an expression for κ_k using an identity $\Delta \boldsymbol{r}^{+}_{k,k+1} \cdot \Delta \boldsymbol{r}_{k,k+1} = d^2_{k,k+1}$:

$$h\kappa_k = \frac{\Delta \boldsymbol{r}^{+}_{i,i+1} \cdot \Delta \boldsymbol{v}'_{i,i+1}\left(t^{+}\right)}{\mu^{-1}_{k,k+1} d^2_{k,k+1}} \tag{24}$$

where $\Delta \boldsymbol{r}^{+}_{j,j+1}$ can be obtained after the holonomic constrained dynamics. An approximate version of Eq.(24) is used in our previous study [23] as

$$h\kappa_k = \frac{\Delta \boldsymbol{r}_{i,i+1} \cdot \Delta \boldsymbol{v}^{*}_{i,i+1}\left(t^{+}\right)}{\mu^{-1}_{k,k+1} d^2_{k,k+1}} \tag{25}$$

after truncating the higher order terms of h^2, equivalently by using $\Delta \boldsymbol{v}'_{k,k+1}\left(t^{+}\right) \simeq \Delta \boldsymbol{v}^{*}_{k,k+1}\left(t^{+}\right)$. In simulations of specific cases, we used Eqs. (14) and (24) to calculate the constraint forces at arbitrary time t with the maximum efficiency of the iteration convergence. But, their run-times are not compared with those of using conventional Eqs. of (16)and (25), because the current research focuses on HF motion and transient forces/torques exerted on local positions of the fiber, instead of comparing numerical algorithms.

2.2.2. Unconstrained and dissipative forces

The gravitational force acting on spheres is an external conservative force that causes constant acceleration in the vertical direction. Hydrodynamic forces as well as torques between spheres in a viscous fluid are intrinsically tensor-wise and dissipative. These unidirectional gravity and tensor-wise hydrodynamic interactions are considered as unconstrained and external as opposed to the internal constraint forces. A chained sphere j experiences a net force as a sum of the gravitational and buoyant forces:

$$\boldsymbol{F}_j^E = \Delta m_j \boldsymbol{g} \tag{26}$$

$$\Delta m_j = m_j - m_f \tag{27}$$

where $m_f = \frac{4\pi}{3} a_j^3 \rho_f$ is the mass of fluid element of density ρ_f of the same volume of sphere j. The many-body hydrodynamic forces exerted on sphere j of linear and angular velocities of $\boldsymbol{v}_j$ and $\boldsymbol{\omega}_j$, respectively, are described as

$$\begin{bmatrix} \boldsymbol{U}^\infty - \boldsymbol{v}_j \\ \Omega^\infty - \boldsymbol{\omega}_j \\ \boldsymbol{E}^\infty \end{bmatrix} = \sum_{k=1}^{N_p} \begin{bmatrix} \boldsymbol{a}_{jk} & \tilde{\boldsymbol{b}}_{jk} & \tilde{\boldsymbol{g}}_{jk} \\ \boldsymbol{b}_{jk} & \boldsymbol{c}_{jk} & \tilde{\boldsymbol{h}}_{jk} \\ \boldsymbol{g}_{jk} & \boldsymbol{h}_{jk} & \boldsymbol{m}_{jk} \end{bmatrix} \cdot \begin{bmatrix} \boldsymbol{F}_k^H \\ \boldsymbol{T}_k^H \\ \boldsymbol{S}_k^H \end{bmatrix} \tag{28}$$

where $\left[\boldsymbol{F}_k^H, \boldsymbol{T}_k^H, \boldsymbol{S}_k^H\right]^{\mathrm{tr}}$ is a column vector of hydrodynamic force, torque, stresslet, exerted on sphere k in the presence of other particles, and the matrix multiplied to $\left[\boldsymbol{F}_k^H, \boldsymbol{T}_k^H, \boldsymbol{S}_k^H\right]^{\mathrm{tr}}$ is called the grand mobility matrix, denoted as $\mathcal{M}_\infty$ [27, 28]. The sub-matrices in Eq. (10) are classified as the second-rank tensors ($\boldsymbol{a}_{jk}$, $\boldsymbol{b}_{jk}$, and $\boldsymbol{c}_{jk}$), third-rank tensors ($\boldsymbol{g}_{jk}$ and $\boldsymbol{h}_{jk}$), and fourth-rank tensor ($\boldsymbol{m}_{jk}$), which obey the symmetry relationship obtained by Lorentz's reciprocal theorem.

In the microhydrodynamics of finite-sized spheres, the disturbance velocity around the

surface S_j of sphere j, is given as

$$\boldsymbol{v}^D(\boldsymbol{r}_j) = \boldsymbol{U}^\infty + \boldsymbol{\Omega}^\infty \times \boldsymbol{x} + \boldsymbol{E}^\infty : \boldsymbol{x} \quad \text{for} \quad \boldsymbol{x} \in S_j \tag{29}$$

where $\boldsymbol{U}^\infty$, $\boldsymbol{\Omega}^\infty$, and $\boldsymbol{E}^\infty$ are the unidirectional velocity, vorticity, and the rate of strain at $\boldsymbol{r}_j$, respectively, of the ambient flow field [27, 28]. In out case, the fluid is stationary, while the HF bundle is periodically moving back and forth in the horizontal direction. Therefore, we set $[\boldsymbol{U}^\infty, \boldsymbol{\Omega}^\infty, \boldsymbol{E}^\infty] = [\boldsymbol{0}, \boldsymbol{0}, \boldsymbol{0}]$. The hydrodynamic forces and torques acting on N_p spheres are calculated by solving the linear system of Eq. (28), given set of $\{\boldsymbol{v}_i, \boldsymbol{\omega}_i\}$ for $i = 1$ to N_p.

2.2.3. Overview of forces and underlying conditions

In this section, we briefly discuss the applicability and limitations of DHD modeling methods, applied to hollow fiber membrane filtration.

Dominant Forces. The dynamics of rigid particles in an unsteady, non-uniform flow is a challenging topic in science and engineering. Microhydrodynamics of particles in viscous fluids requires an in-depth understanding of fluid dynamics, particle motion, and particle-fluid interactions. Reynolds number is often used to classify this fundamental problem into several categories. To the best of our knowledge, the available literature is limited to the hydrodynamics of multiple particles in a low Reynolds number regime, the inertial motion of a single spherical particle in unsteady flows of high Reynolds numbers, and the multi-physics turbulent flows often including heat transfer phenomena. An equation of motion for a single sphere in an arbitrary flow consists of driving forces of various origins, which include [29]: the gravitational/buoyant force $\boldsymbol{F}^G$, Stokes' drag force $\boldsymbol{F}^S$ proportional to the particle velocity relative of the undisturbed velocity $\boldsymbol{u}$ and its Laplacian; velocity gradient force $\boldsymbol{F}^u$ ($\propto D\boldsymbol{u}/Dt$), described using the substantial gradient of $\boldsymbol{u}$ in Eulerian picture; added mass force $\boldsymbol{F}^m$, including the inertia of the relative velocity and the Laplacian of $\boldsymbol{u}$ at the center of the particle in its imaginary absence; and finally the Basset history term $\boldsymbol{F}^B$ [30], influencing the history of the particle's relative acceleration to the particle's current motion.

When constraint forces are included, the significance of individual forces described above varies.

Viscous Forces versus the Basset History Force. We incorporate the dissipative hydrodynamics (as a poly-disperse extension of the Stokesian dynamics) with the RATTLE-based constrained algorithm to simulate the flexible motion of connected spheres. In the present hydrodynamic circumstances, we adopted reasonable approximations as follows. The gradient force $\boldsymbol{F}^u$ of the undisturbed velocity $\boldsymbol{u}$ is negligible because the fiber moves initially in a stationary ambient fluid and the fluid motion due to the fiber's translational motion is secondarily induced. The added mass force $\boldsymbol{F}^m$ is also discarded by estimating the equivalent frequency ω_s for the Stokes' drag as compared to the oscillation frequency ω listed in Table 1. We let the particle velocity and acceleration have approximate magnitudes of $a_p\omega_s$ and $a_p\omega_s^2$, respectively, and calculate the representative frequency as $\omega_s = 6\pi\mu a_p/m_f$ where $m_f = \frac{4\pi}{3}a_p^3\rho_f$ is the fluid mass occupying the particle volume. We estimate ω_s as least one order of magnitude larger than the rack oscillation frequency ω. Finally, we assume that the Basset history force $\boldsymbol{F}^B$ [30], requiring the time integration of the relative acceleration from $t = -\infty$, is insignificant because the individual particle trajectory is primarily governed by the hydrodynamic drag and constraint forces.

Model Applicability to a Long Fiber. Stokesian dynamics incorporate the far-field approximation's grand mobility and updates its inverse matrix by adding pair-wise resistance submatrices. Stokesian dynamics' accuracy is improved from the vector-wise drag force applied to individual particles to the tensor-wise many-body forces/torques. Applications of But Stokesian dynamics is, however, limited to a low particle Reynolds number. Therefore the governing equation of Stokesian dynamics does not include all the forces described above, except the gravitational/buoyant force. To the best of our knowledge, the holonomic constraints were barely studied in hydrodynamics literature of colloids and nanoparticles, used for the microhydrodynamics, to maintain multimers' geometrical properties (such as dimers, trimers, and small aggregates and chains) invariant at any time t. By incorporating the

basic formalism of Stokesian dynamics, the present study applies dissipative hydrodynamics to investigate the absolute and relative significance of the tensile and compressive forces exerted on each of N_p spheres forming a long change.

Fluid-Solid Interaction. The governing equation for the constrained motion of spheres follows the essential condition of the Stokesian dynamics that the fluid is stationary, the particle Reynolds number is small, and the fluid-particle interactions are negligible. Because the fiber-forming spheres move primarily in $\pm x$ direction, the sum of individual particle's linear momentum is finite. Therefore, the periodic fiber motion induces fluid motion to cancel out the moving fiber's linear momentum. Although the fluid-solid interactions are seemingly significant, the fluid motion responsively to the fiber motion must follow similar oscillatory patterns, of which the mean linear momentum is negligible. On average, we assumed that the drag forces exerted on the moving fiber are not sensitively influenced by the fluid-solid interactions.

Effects of the Initial Configuration. In this MBR application, the fiber motion can be seen as forced oscillation led by the reciprocating rack. The moving rack determines two end-positions of the fiber at any time t, anchored to the rack's bottom and ceiling. The gravitational force acting on N_p spheres is externally applied, but the accumulated gravitational compression is transferred through neighboring spheres in contact. Because the hydrodynamic forces/torques are tensor-wise interactions, horizontally pulled spheres (as parts of the chain) can experience vertical lifting forces and, at the same time, transmit less gravitational compression to its touching neighbors. In summary, the viscous drag force dissipates the fiber's kinetic energy, produced by the motored rack motion. The hydrodynamic drag and gravitation are balanced with the constraint forces that make the history effect less critical. In this case, the specific fiber structure is almost instantaneously formed because the hydrodynamically dragged chain responds to the compressive and tensile forces by developing the constraint forces. Therefore, the effects of initial configuration on the dynamic chain's time evolution seem negligible, as observed in this software package's developing phase.

Effects of the Permeate Flux. The suction pressure (of maximum 1 atm) can indeed generate the permeate flow from the exterior to the hollow fiber's interior. In most HF membrane separations, the flux is an order of 1 to 10 μm/s, which is at least three to four orders of magnitude smaller than the rack speed. The interior is already filled with pre-penetrated water so that the permeate flow entering the fiber's lumen spaces does not influence the mechanical properties of the fiber during the reciprocating motion. Therefore, we assume that the permeate flux neither alters the no-slip boundary condition on the fiber surfaces nor change the disturbance flow-field outside the HF membrane.

2.2.4. Grand governing equations

Many-body interactions using Stokesian dynamics. The grand governing equation for the motion of sphere j is then written as

$$\begin{bmatrix} m_j & 0 \\ 0 & I_j \end{bmatrix} \begin{bmatrix} \boldsymbol{a}_j \\ \boldsymbol{\alpha}_j \end{bmatrix} = \begin{bmatrix} \boldsymbol{F}_j^H \\ \boldsymbol{T}_j^H \end{bmatrix} + \begin{bmatrix} \boldsymbol{F}_j^E \\ 0 \end{bmatrix} + \begin{bmatrix} \boldsymbol{F}_j^C \\ 0 \end{bmatrix} \tag{30}$$

where $I_j = \frac{2}{5} m_j a_j^2$ is the mass moment of inertia of sphere j, $\left[\boldsymbol{F}_j^H, \boldsymbol{T}_j^H\right]^{\mathrm{tr}}$ is the hydrodynamic force/torque obtained by solving Eq. (28), $\left[\boldsymbol{F}_j^E, 0\right]^{\mathrm{tr}}$ and $\left[\boldsymbol{F}_j^C, 0\right]^{\mathrm{tr}}$are external and constraint forces, respectively. Therefore, Eq. (30) can be considered as multi-sphere, tensorwise Langevin's equation for multiple spheres in a viscous fluid. Because the external and constraint forces are the central forces, their torques do not exist, but the hydrodynamic torque $\boldsymbol{T}^H$ in Eq. (28) influences the linear velocity $\boldsymbol{v}$ through the grand mobility matrix for the N_p connected spheres.

Variable Time Step. Substitution of the linear and angular acceleration of Eq. (30) into the time evolution equations requires a specific value of the time step h. We determined the time step by trial and error to limit the maximum displacement within a one-time step as a fraction of the particle radius. We determined the initial value of h of an order of $O\left(10^{-5}\right)$ s as a well-educated guess estimated by precedent trial simulations. Throughout

simulations, h had a range from 10 to 20 microseconds and the total number of time steps ranges from 10K to 20K per reciprocation period. During simulations, the maximum force $F_{\max}$ (in magnitude) exerted on one of N_p particles was recorded, and h was intermittently adjusted by keeping the maximum distance traveled by a particle from time t to $t+h$ much smaller than the particle radius: $F_{\max}h^2/2m \ll a_p$. During simulations, h was initially set small enough and adjusted gradually. The purposes of using this variable h is not only to minimize the error accumulation but also to maintain the numerical convergence during the iterative calculations of Lagrange multipliers $\boldsymbol{\lambda}$ and $\boldsymbol{\kappa}$.

2.3. Simulations

2.3.1. Hollow fiber configurations

Table 1 shows specific simulation parameters that represent the real application of the HF dynamics in a membrane bioreactor. Two representative HF lengths, i.e., l_f =1,000 mm and 2,000 mm long, are modeled in this study. Here, stack ratio R_{st} is defined as

$$R_{\text{st}} = 1 - \frac{H}{l_f} \tag{31}$$

where H is the stack height, i.e., the surface-to-surface distance between the top and bottom plates of the rack. In this study, the stack ratio R_{st} is set as 0.2%. The rack oscillation is characterized using frequency $\omega = 0.46$ Hz and amplitude A (the maximum displacement of the stack in each side) set as 6.0 % of the stack height, i.e., $A = 0.06\,H$. The fiber material of thickness $a_f - b_f$ consists of the solid and void parts and their relative portion is described using the fiber porosity ϵ. While the HFs are used for membrane separation, the rejection of suspended solids occurs on the outer surfaces of the fibers. Due to the pressure gradient from the shell to the lumen regions of the fiber, water occupies the cylindrical lumen space and the porous spaces of the fibers. Hence, per length, mass of a submerged fiber consists of solid mass of the fiber and water mass inside the lumen and porous spaces. In our study, a cylindrical segment of the long HF of length $2a_f$ and thickness $a_f - b_f$ is replace by a solid

sphere of radius a_f of the equal mass, as shown in Fig. 3.

Then, we let m_s as the mass of a water-filled fiber segment of length and diameter of both $2a_f$, it is

$$m_s = 2a_f \left[\pi b_f^2 \rho_w + \pi(a^2 - b^2) \cdot \bar{\rho}_f\right] \tag{32}$$

$$\bar{\rho}_f = \epsilon\rho_w + (1-\epsilon)\,\rho_s \tag{33}$$

where ρ_w and ρ_s are densities of solvent (water) and the solid part of the fiber material (excluding the void spaces), and $\bar{\rho}_f$ is the effective density of the HF, whose void and lumen spaces are filled with water. We also define m_p as mass of the equivalent sphere of radius a_f, such that

$$m_p = \frac{4\pi}{3} a_f^3 \rho_p \tag{34}$$

where ρ_p is the mass density of the equivalent sphere. By equating Eqs. (32) and (34), we have

$$\rho_p = s_p \rho_w \tag{35}$$

$$s_p = \frac{3}{2}\left[\hat{b}^2 + (1-\hat{b}^2) \cdot \bar{s}_f\right] \tag{36}$$

where $\hat{b} = b_f/a_f$ is the ratio of the inner to the outer radius of the HF, and $\bar{s}_f = \bar{\rho}_f/\rho_w$ and s_p are specific gravity of the water-filled HF of thickness $a_f - b_f$ and that of the equivalent sphere, respectively.

Table 2 shows material properties of polyvinylidene fluoride (PVDF) and polyethylene terephthalate (PET) membranes and their equivalent spheres. The solid mass density of PVDF is higher than that of PET, but the HFs made of PVDF is much thinner than that of PET. Having the similar porosity $\epsilon = 65.0\,\%$, the equivalent spheres of PVDF and PET have almost equal mass, i.e., $\sim 7.0\,\mathrm{mg}$, and hence equal specific gravity, s_g.

2.3.2. Stack oscillation

A HF is modeled as a chain consisting of N_p spherical particles. All the spherical particles forming a chain has the same radius i.e., $a_1 = a_2 = \cdots = a_k = \cdots = a_N$, denoted as a_p and set equal to the fiber's outer radius a_f. The first and the last particles of index 1 and N_p, respectively, are attached to the bottom and top surfaces of the moving rack, respectively. The coordinates of sphere 1 and N_p are assigned as

$$\boldsymbol{r}_1 = \left(A\left(1 - \cos\omega t\right), 0, 0\right) \tag{37}$$

$$\boldsymbol{r}_N = \left(A\left(1 - \cos\omega t\right), 0, H - 2a_p\right) \tag{38}$$

from which, their velocities and accelerations are calculated as

$$\boldsymbol{v}_1 = \boldsymbol{v}_N = \left(A\omega \sin\omega t, 0, 0\right) \tag{39}$$

and

$$\boldsymbol{a}_1 = \boldsymbol{a}_N = \left(A\omega^2 \cos\omega t, 0, 0\right) \tag{40}$$

respectively.

2.3.3. Sample simulation using short chains

In this section, we use a short sample fiber, consisting of $N_p = 100$ spheres, as shown in Fig. 4, to illustrate the dynamic system. Full-scale simulation results are discussed in the following sections. The bottom and top plates consist of a 13 by 7 array of spheres, as shown in Fig. 4(a) and (b), having twice the radius of the unit spheres belonging to the chain. These plates represent surfaces of the moving rack and provide hydrodynamic shear stresses on spheres near the plates [26]. The total number of particles is, therefore, $N_p\,(= 100) + (7 \times 13) \times 2 = 282$, where the N_p value will be replaced by 500 and 1,000 for 1 and 2 meter long HFs, respectively. Particle 1 and 100 are, in principle, moving at

the same velocity of the bottom and top plates, described using Eq. (39). Specifically, Fig. 4(a) shows the overview of the initial state (at $t = 0$) for the 100 spheres, forming a highly skewed triangular shape. The center of the chain is positioned at the slight left-hand side of the vertical z-axis (marked in blue). Fig. 4(b) shows a fiber shape at a short time later ($t = 0.0783\,\mathrm{s} = 0.0360\,\tau$), where the top and bottom halves of the chain passed and left behind the fixed z-axis, respectively. The hydrodynamic force initially exerted on the chain pulls forward the top-half of the chain, while the gravitational force pushes the bottom-half of the chain slightly behind the moving front.

Spheres as continuous segments of fibers experience the hydrodynamic drag forces on the horizontal direction and cumulative gravitational forces transmitted through the holonomic constraints of the nearest neighbors in the downward direction. Figs 4(c) and (d) show closer views of (a) and (b), respectively. Individual sphere colors are to visually track the dynamics of each sphere. On each sphere, six small dark tips are attached to visually investigate negligible angular motion of spheres using consecutive snapshot images and animation movies. Although this chain of 100 spheres show the representative motion of a hanging HF, we found that this chain is not long enough to show physically meaningful turning effects on the fiber hydrodynamics. On the other hand, the visualization of the longer chains is challenging because their aspect ratio, i.e., length divided by diameter, is extremely large, which is equal to the number of spheres, N_p. In simulations of realistic cases, as listed in Table 1, local force/torque distributions are discussed in detail without the chain visualization.

3. Results and Discussion

3.1. Overview

In this section, computational hydrodynamics results are discussed for the dynamics of chains of 500 and 1,000 spheres for 1.0 m and 2.0 m long HF membranes, respectively. Specific parameters used are listed in Tables 1 and 2. The goal of this computational study is to investigate specific forces applied to local segments of the HF, represented as a connected

chain of individual, equal-sized spheres. As noted above, the types of forces acting on each N_p spheres include the gravitational (external and conservative), hydrodynamic (external and dissipative), and constraint (internal with a zero resultant) forces. The calculation of the gravitational force acting on each sphere is straightforward. The accumulation of the downward force is through the holonomic constraint, and the sphere chain forms a force chain [31]. Computation of many-body hydrodynamic tensors, i.e., creating the grand mobility matrix and solving the linear system, often requires high-performance hardware systems with large memory required. Each constraint force is primarily developed to maintain the shape of the sphere-connecting chain but often strong enough to provide mechanical stresses on the fiber. On the other hand, the evaluation of the constraint forces requires a significant amount of computational resources for the iterative convergence of the Lagrange multipliers of λ_j and κ_j for $j = 1$ to N_p of the holonomic and non-holonomic constraints of Eqs. (1) and (17), respectively. Calculation of $\boldsymbol{\lambda}$ vector of N_p elements means simultaneously satisfying all the holonomic constraints of Eq. (1) using specific numerical algorithms. Because the unconstrained evolution breaks, in principle, N_p holonomic constraints, the subsequent constraint evolution should re-satisfy the temporarily broken constraints by using iterative algorithms. However, the conventional constrained dynamics at the molecular level has been used mainly to simulate the dynamic and material properties of rigid compound molecules.

The one-side constraint force acting on sphere j by one of its neighbors, let's say sphere $j + 1$, is perfectly canceled out by the constraint force acting on sphere $j + 1$ by sphere j to satisfy Newton's third law. But constraint-force magnitudes are strongly related to the long-term durability and mechanical stability of the HF membrane, because the constraint forces create both tensile and compressive stresses. In this study, a HF membrane, modeled as a sphere-connecting chain, is conceptually characterized as flexible in full-length scale but rigid in diameter scale. We calculated individual components of forces, exerted on all aligned spheres, and more importantly showed the effects of the reciprocating motion on the periodicity of exerted forces on spheres. In these sections, computational hydrodynamics

results are discussed for dynamics of chains consisting of 500 and 1,000 spheres, mimicking 1.0 m and 2.0 m long HF membranes, using parameters specified in Tables 1 and 2, respectively.

3.2. Dynamic chain configurations

The hydrodynamic chain simulations were conducted from $t = 0$ to $t = 1.5\,\tau$, where τ is the period of cassette oscillation, calculated as $\tau = \omega^{-1} = 2.174\,\text{s}$. Fig. 5 shows sequential snapshots of the dynamic chain configurations at five different time steps from $t = 0$ to τ. Initially, the chain has a highly skewed, equilateral triangle configuration, shown on the leftmost side of Fig. 5(a) (similar to Fig. 4(a)). From the initial time to a quarter period, the chain moves from the left to the right sides of Fig. 5. As the chain follows the rack, the chain configuration at $t = 0.25\tau$ (of (b) 5) shows the open-parenthesis shape. Configuration (c) is made when the fiber starts switching directions, after the rack stops at the rightmost position at $t = 0.5\tau$. The chain position moves from (c) at $t = 0.5\tau$ to (d) at $t = 0.75\tau$, keeping the dynamic shape of a closing parenthesis. The chain configurations of (b) at $t = 0.25\tau$ and (d) at $t = 0.75\tau$ have coinciding top and bottom positions and form a symmetricity about the vertical line connecting the top and bottom spheres. After the rack switches directions to the right after $t = \tau$, the chain configuration changes to open parenthesis of (e), similar to (b), from the closed parenthesis of (d). The simulation continues from time $t = \tau$ to 1.25τ when the chain passes the central zone for the second time, and to 1.5τ until the chain reaches the rightmost position, of which configurations are identical to those of (b) at $t = 0.25\tau$ and (c) at $t = 0.5\tau$, respectively. Chain configurations at $t = 1.25\tau$ and 1.5τ are not shown in Fig. 5.

3.3. Force analysis

In this work, four cases are studied to perform a comparative analysis on short and long chains made of PVDF and PET. Tables 1 and 2 show that both PVDF and PET membranes have approximately the same specific gravity, because the PET HF membrane is thicker than PVDF HF, but it has a lower solid density. Porosities of both HF membranes

were assumed to be equally 0.65. We found that the forces exerted on the PET membrane are quantitatively similar to those on PVDF. Our force analysis, therefore, focuses on the PVDF membranes of two different lengths: 1 and 2 meters. Simulation results of the PET membranes are included in the Appendix. Eq. (6) represents the constraint forces exerted on sphere k, as a superposition of the backward force by sphere $k-1$ and the forward force by sphere $k+1$, denoted $\boldsymbol{f}_b^k = \lambda_{k-1}(\boldsymbol{r}_{k-1} - \boldsymbol{r}_k)$ and $\boldsymbol{f}_f^k = \lambda_k(\boldsymbol{r}_{k+1} - \boldsymbol{r}_k)$, respectively. Note that $(\boldsymbol{r}_{k\pm1} - \boldsymbol{r}_k)$ indicates the relative position from sphere k to sphere $k \pm 1$ and Lagrange's multipliers λ_{k-1} and λ_k determines magnitudes and directions of $\boldsymbol{f}_b^k$ and $\boldsymbol{f}_f^k$. Although the net constraint force effectively exerted on sphere k is $\boldsymbol{f}_s^k = \boldsymbol{f}_b^k + \boldsymbol{f}_f^k$, $\boldsymbol{f}_b^k$ and $\boldsymbol{f}_f^k$ are internal forces for sphere k to resist the compressive or tensile stresses from sphere $k-1$ and $k+1$, respectively.

In the following sections, transient force profiles exerted on a 1 m PVDF HF membrane in the x- and z-directions are shown in Figs. 7 and 8, respectively, and those of a 2 m PVDF HF are in Figs. 10 and 11, respectively. The force profiles are obtained at 654 time steps, i.e., 109 time steps for a quarter period, denoted $\tau_{1/4}$, and fiber snapshots at every quarter period from $t = 0$ are visualized and discussed.

3.3.1. PVDF membrane of 1 meter

Fig. 6 shows snapshot series of a 1 m PVDF HF chain during the 1.5 period. Fiber configurations during the first half-period ($0 < t < 0.5\tau$) are very similar to those during the third half period ($\tau < t < 1.5\tau$). In each half period seven or eight snapshots were individually taken and overlaid onto the snapshot of the initial fiber configuration. The configuration similarity between the first and third half periods implies the qualitatively and quantitatively similar force fields applied to the fiber in the interval of one period.

Fig. 7 shows x-directional profiles of the constraint and resultant forces exerted on a 1 m PVDF HF, consisting of 500 equivalent spheres, where the resultant force indicates a net force, as a superposition of all non-vanishing forces exerted on a sphere. The forward and backward constraint forces in the x-direction, as shown in Figs. 7 (a) and (b), respectively,

appear anti-symmetric at each time step in terms of their magnitudes and signs. Interestingly, Fig. 7 (a) shows, at $t = \tau_{1/4}$, groups of spheres of indices $k \gtrsim 100$ and $k \lesssim 100$ undergo the positive and negative forward constraint force $\boldsymbol{f}_f^k$, respectively, being pulled forward to the positive x-direction and pushed back to the negative x-direction, respectively. Spheres of indices $k \approx 100$ undergo much less forward and backward constraint forces. The backward constraint forces $\boldsymbol{f}_b^k$, shown in Fig. 7 (b), have similar patterns to Fig. 7 (a), in opposite directions. Fig. 7 (c) shows the sum of the forward and backward forces, denoted $\boldsymbol{f}_{s,x}$, which is the effective constraint force developed by sphere k to maintain the embedded constraints. Because $\boldsymbol{f}_f^k$ and $\boldsymbol{f}_b^k$ have similar magnitudes but opposite signs, their resultant force $\boldsymbol{f}_{s,x}$ has a much smaller magnitude than those of $\boldsymbol{f}_f^k$ and $\boldsymbol{f}_b^k$. Furthermore, each of $\boldsymbol{f}_f^k$ and $\boldsymbol{f}_b^k$ is the actual constraint forces developed by sphere k to maintain the chain structure, and $\boldsymbol{f}_{s,x}$ is effectively used to satisfy the constraints of Eqs. (1) and (17) instantaneously. In Fig. 7 (c), the odd and even time indices mean that the fiber positions are near the central and edge zones, respectively. The magnitude of the resultant constraint force in the x-direction $\boldsymbol{f}_{s,x}$ has larger magnitude when the fiber is turning directions on each side, rather than passing the central region at a faster speed. Notably, the zero-force region of $k \approx 100$ in the forward and backward forces disappears in the net constraint force profile, as shown in the insert of Fig. 7 (c). There are a few interesting things in the insert of Fig. 7 (c). A small '>' shape kink of the profile $\boldsymbol{f}_{s,x}$ at $t = 0$ is ascribed to the initial chain configuration of the perfect triangular shape as shown in Fig. 5(a). The net constraint force profile near the top, shown in Fig. 7 (c) insert, has similar patterns to those of the backward constraint forces near the bottom parts of the HF, where sphere indices $k \leq 100$. Force units of Fig. 7 (c) and its insert are μN and nN. The net constraint forces exerted on the bottom 4 percent of the HF, i.e., sphere index $k \leq 20$, are approximately two orders of magnitude larger than those above sphere $k \geq 20$. Fig. 7 (d) shows the resultant force on the x-direction as a sum of all x-directional forces exerted on the fiber. The trend of the net force profile with respect to the time index is similar to that of Fig. 7 (c). Only a few spheres near the bottom experience

much stronger force than other spheres above them. At time steps of $\tau_{1/4}$, $3\tau_{1/4}$, and $5\tau_{1/4}$, i.e., when the fiber passes the central zone, the net-force magnitudes suddenly increase from the bottom and gradually decrease toward the ceiling of the cassette. On the other hand, at time steps of $2\tau_{1/4}$, $4\tau_{1/4}$, and $6\tau_{1/4}$, when the fiber stops and turns to the opposite direction, $\boldsymbol{F}_x$ profile shows a zig-zag pattern that sphere 3 experiences the strongest net force and sphere 2 undergoes the resultant force less strongly than that of sphere 2 in the opposite direction. Spheres of indices $k \geq 4$ experience the net force, gradually decreasing toward the ceiling of the cassette. Interestingly, forward/backward constraint, net constraint, and resultant forces, exerted near the bottom, have magnitudes of orders of $O\left(10^0\right)$, $O\left(10^{-1}\right)$, and $O\left(10^{-2}\right)\mu$N, respectively.

Fig. 8 shows z-directional profiles of the constraint and total forces, exerted on the same HF of Fig. 7. In the LENA system, the gravitational and buoyant forces exerted on each PVDF sphere are $F_g = -\frac{4\pi}{3}a_f^3 g S_g = -67.679\,\mu$N and $F_b = +\frac{4\pi}{3}a_f^3 g = +41.092\,\mu$N, respectively, in the z-direction, of which the sum is -26.587 μN. In Figs. 8(a) and (b), forward and backward constraint forces in the z-direction are unconditionally positive and negative, respectively. The positive forward constraint force indicates that sphere k is pulled upward by the positive forward constraint force by sphere $k+1$, and at the same time the negative backward constraint force is for sphere $k-1$ to pull down sphere k. The net gravitational force, denoted $\Delta F_{GB} = F_G - F_B$, has a magnitude within the range of an order of $O\left(10\right)$ for forward and backward constraint forces. Because the z-directional constraint forces should balance ΔF_{GB}, their magnitude is about ten times the x-directional constraint forces of Figs. 7(a) and (b). In Fig. 8(c), similar to the net constraint force in the x-direction in Fig. 7(c), $\boldsymbol{f}_{s,z}$ has a much smaller magnitude than those of $f_{f,z}$ and $f_{b,z}$ because the z-directional constraint forces should balance ΔF_{GB}. The individual (either forward or backward) constraint, net constraint, and resultant forces have magnitudes of orders of $O\left(10^1\right)$, $O\left(10^{-1}\right)$, and $O\left(10^{-2}\right)$, respectively. In Fig. 8 (d), the resultant force profiles at the odd and even time indices have positive and alternating signs, respectively. When the

fiber passes the central zone moving to the right at $t = \tau_{1/4}$ and $5\tau_{1/4}$ and to the left at $t = 3\tau_{1/4}$, the fiber has maximum speed with minimum magnitude of acceleration in the x-direction. Therefore, the gravitational forces are accumulated over the spheres so that the bottom spheres experience much stronger downward forces, balanced by the net constraint force in the z-direction. On the other hand, when the fiber turns directions on each side, sphere 2 experiences the net downward force because it plays the role of transient anchor for the fiber to alternate directions.

3.3.2. PVDF membrane of 2 meters

In this section, we specifically discuss the effects of fiber length by comparing the results of a 2 m PVDF HF membrane with those of Figs. 7 and 8. Firstly, Fig. 9 shows snapshot series of a 2 m PVDF HF chain during the 1.5 period. Similar to Fig. 6, in each half period, seven or eight snapshots were individually taken and overlaid onto the initial snapshot (at $t = 0$). Unlike Fig. 6(c), fiber configurations during the third half period ($\tau < t < 1.5\tau$) are different from those of the first half period ($0 < t < 0.5\tau$), because they are closer to those of the second half-period ($0.5\tau < t < \tau$). When the second half period has ended, the left-most fiber configuration of Fig. 9(b) seems to be pushed to the right without the horizontal flipping of the configuration that occurred near $t = 0.5\tau$, i.e., the rightmost configurations of Figs. 9(a) and (b). This broken periodicity can be possibly explained by influences of the heavier mass due to the doubled length than that of 1 m PVDF HF of Fig. 6.

Fig. 10 shows x-directional profiles of the constraint and total forces, exerted on a 2 m PVDF HF, consisting of 1,000 equivalent spheres, to be compared with Fig. 7 for 1 m PVDF HF. The magnitudes of the forward and backward constraint forces in the x-direction, shown in Figs. 10(a) and (b) are approximately two orders of magnitude larger than those shown in Figs. 7(a) and (b), respectively. The zones of zero forward/backward constraint forces also appear near the bottom 20 percent near sphere indices $k \approx 200$ in Figs. 10(a) and (b), but the trend is less apparent and symmetrical as compared to those of Figs. 7(a) and (b), respectively. In Fig. 10(c), profiles of the net constraint forces appear sequentially ordered

between sphere 5 and 20, while Fig. 7(c) shows that encapsulation of the net constraint force profiles at $t = \tau_{1/4}$, $3\tau_{1/4}$, and $5\tau_{1/4}$ by those at $t = 2\tau_{1/4}$, $4\tau_{1/4}$, and $6\tau_{1/4}$. This sequential ordering of x-directional net forces in Fig. 10(c) also appears in Fig. 10(d). The resultant force profiles near the bottom are dominantly controlled by net constraint forces of a 2 m long PVDF HF, as already shown between Fig. 7(c) and (d).

The reciprocating motion of the HF can be viewed as a forced oscillation in classical mechanics. If a stretchable string of a musical instrument) is considered, this gravity accumulation is not dominant as the vertical gravitation is perpendicular to the horizontal string oscillation. When the cassette is moving slow enough, then the net gravitational force applied to the bottom particle (that the bottom end of an HF experience) must be close to the total weight above the bottom location. If the cassette moves fast, then the effect of gravity on the fiber shape would be less. When the rack speed is at the maximum, passing the midpoint, the fiber will make either open or close parenthesis shape. In this case, the pair of constraint forces acting on sphere k from sphere $k-1$ and $k+1$ can be much stronger than the gravity to cancel out the hydrodynamic drag to disperse connected particles. A faster relative velocity between the fiber element (i.e., sphere) and the stationary fluid will make some spheres experience tensile forces only, i.e., pulled by the two adjacent spheres in the opposite directions. Constrained forces between two adjacent spheres are entirely canceled each other at any time, but the magnitude of each contribute to keeping the fiber length unchanged. The gravitational and hydrodynamic forces are mostly perpendicular to each other except when the fiber turns the moving direction at each end. The constrained forces are instantaneously generated to keep the chain configuration by balancing the gravity, and hydrodynamic forces in the direction made by connecting centers of the two spheres. Let's consider a probe particle, selected as the 300th sphere (from the bottom) of each of the 1 m and 2 m fiber cases. This probe particle in 1 m and 2 m fibers has 200 and 700 spheres connected above it. The probe sphere of 2 m fiber may experience 3.5 times stronger compression than in the 1 m fiber. This ratio heavily depends on the particle velocity in

x-direction because a faster rack speed will provide a stronger drag force (tensor-wise) so that the vertical force induced by the gravitation is reduced.

Fig. 11 shows z-directional profiles of the constraint and total forces, exerted on the same HF of Fig. 10. Figs. 11(a) and (b) show more asymmetric patterns in the sequential profiles of the forward and backward constraint forces, as compared with those in Figs. 8(a) and (b), respectively. The forward and backward constraint forces in the z-direction of a 2 m long PVDF HF membrane have approximately one order of magnitude larger than those of a 1 m PVDF HF membrane (of Fig. 8). Doubling the fiber length increases the individual constraint forces by approximately ten times in both x- and z-directions, which, in our opinion, stems from the accumulative gravitational force, exerted on sphere k by ones above it, i.e., spheres of indices ranging from $k+1$ to N_p. Fundamental analyses of the gravitational compression on packed spheres can be found elsewhere [31, 32]. The insert of Fig. 11(c) confirms the mostly positive net constraint force in the z-direction of an order of $O\left(10^{-1}\right)$ μN, except the vicinity of the bottom surface, as already indicated by the discussion of Fig. 7(c). The zigzag patterns shown in time profiles 2, 4, and 6 in Fig. 8(c) appears to become universal in Fig. 11(c), in which most of $\boldsymbol{f}_{s,z}$ profiles show horizontally flipped S curves. The net constraint force profiles show a seemingly cyclic pattern from the time index 1 to 6, but this does not mean the periodicity of the z-directional net constraint force. Similar patterns of force profiles appeared in Figs. 11(c) and (d), additionally confirming that the net constraint force dominantly influences the resultant force. The bottom 1 percent portion of the fiber in length experiences the highest net forces in x- and z-directions for both the 1 m and 2 m PVDF HF membranes. Overall, the 2 m long PVDF HF membrane shows less symmetrical patterns in the net constraint and resultant forces.

The orders of magnitudes of exerted forces on PVDF HF membranes are listed in Table 3, which provides quantitative force analysis regardless of the HF length, as follows:

1. The forward and backward constraint forces in the z-direction is one order of magnitude larger than those in the x-direction.

2. The net constraint forces in both x- and z-directions are one order of magnitude smaller than individual constraint forces in the x-direction.
3. The resultant forces in both x- and z-directions are two orders of magnitude smaller than individual constraint forces in the x-direction.

These analyses are also valid for PET HF membranes, of which simulation results are included in the Appendix.

4. Concluding Remarks

In this work, forces exerted on the 1 m and 2 m long PVDF HF membranes were investigated using the standard modeling technique of dissipative hydrodynamics (based on the grand mobility scheme of Stokesian dynamics). While there is no representative tool to simulate dynamics of a hollow fiber as a flexible body of finite length, we applied the dissipative hydrodynamics for polydispersed particle systems. A HF of length l_f and outer diameter d_f is modeled as a chain of connected spheres of the same diameter and equal mass of a cylindrical segment of length d_f. The constrained dynamics employed is based on the RATTLE algorithm, which satisfy at an arbitrary time the holonomic and non-holonomic constraints related to center-to-center distance and orthogonality between changes in the displacement and velocity between two adjacent spheres. Profiles of forces exerted on PVDF HFs of 1 m and 2 m in length were calculated using the hydro-RATTLE algorithm. The net gravitational force, i.e., the gravity subtracted by the buoyant force of a PVDF HF segment, is of an order of $O\,(10)$ μN, which is accumulated downward through connected spheres. The forward and backward constraint forces show symmetric profiles, indicating that they have similar magnitudes, applied in opposite directions. Therefore the net constraint forces are at least one order of magnitude smaller than each of the forward and backward constraint forces that maintain the sphere connectivity. Although the net constraint force is developed to satisfy the constraints instantaneously, the magnitude of both constraint forces need to be accurately quantified to design the HF material for mechanical stability. Due to the effects of

accumulated gravitational forces through the fiber, only 1 percent of the fiber at the bottom experiences the largest forces in both the x- and z-directions. The y-directional forces were calculated as several orders of magnitude smaller than those of x- and z-directional forces, which allowed us to assume that sphere twisting is not dominant most times, except when the fiber is switching directions on each end. A longer fiber not only increases the tensile and compressive forces accumulated near the bottom of the fiber, but also provide stiff configurations that can preclude regular reciprocating patterns. Due to the computational limitation, this work studied only one fiber consisting of 500 and 1,000 equivalent spheres during the 1.5 period. In reality, the inter-fiber hydrodynamic interactions also play a significant role in the dynamic formation of HF configurations. More sophisticated modeling is required to rigorously predict the dynamics of multiple flexible fibers attached to a cassette, especially at an arbitrary particle Reynolds number.

Acknowledgment

This work was financially supported by the national R&D project of "Development of 1 MW OTEC demonstration plant (5/6)" (PMS4320) funded by the Ministry of Oceans and Fisheries of the Republic of Korea and "Industry-Academia Collaboration Program" of Kolon Industry.

References

[1] E. McAdam, S. Judd, A review of membrane bioreactor potential for nitrate removal from drinking water, Desalination 196 (1-3) (2006) 135–148. doi:10.1016/j.desal.2006.03.008.
URL https://linkinghub.elsevier.com/retrieve/pii/S0011916406004280

[2] A. L. Smith, L. B. Stadler, N. G. Love, S. J. Skerlos, L. Raskin, Perspectives on anaerobic membrane bioreactor treatment of domestic wastewater: A critical review, Bioresource Technology 122 (2012) 149–159. doi:10.1016/j.biortech.2012.04.055.
URL https://linkinghub.elsevier.com/retrieve/pii/S0960852412006608

[3] H. Lin, W. Peng, M. Zhang, J. Chen, H. Hong, Y. Zhang, A review on anaerobic membrane bioreactors: Applications, membrane fouling and future perspectives, Desalination 314 (2013) 169–188. doi:10.1016/j.desal.2013.01.019.
URL https://linkinghub.elsevier.com/retrieve/pii/S0011916413000386

[4] R. W. Holloway, A. Achilli, T. Y. Cath, The osmotic membrane bioreactor: a critical review, Environmental Science: Water Research & Technology 1 (5) (2015) 581–605. doi:10.1039/C5EW00103J.
URL http://xlink.rsc.org/?DOI=C5EW00103J

[5] Y. Hu, X. C. Wang, H. H. Ngo, Q. Sun, Y. Yang, Anaerobic dynamic membrane bioreactor (AnDMBR) for wastewater treatment: A review, Bioresource Technology 247 (2018) 1107–1118. doi:10.1016/j.biortech.2017.09.101.
URL https://linkinghub.elsevier.com/retrieve/pii/S0960852417316668

[6] L. Goswami, R. Vinoth Kumar, S. N. Borah, N. Arul Manikandan, K. Pakshirajan, G. Pugazhenthi, Membrane bioreactor and integrated membrane bioreactor systems for micropollutant removal from wastewater: A review, Journal of Water Process Engineer-

ing 26 (2018) 314–328. doi:10.1016/j.jwpe.2018.10.024.
URL https://linkinghub.elsevier.com/retrieve/pii/S2214714418306329

[7] A. S. Kim, W. Oh, H.-S. Lee, S. Cha, H.-J. Kim, Perspective of membrane distillation applied to ocean thermal energy conversion, IDA Journal of Desalination and Water Reuse 7 (1-4) (2015) 17–24. doi:10.1179/2051645215Y.0000000002.
URL http://www.tandfonline.com/doi/full/10.1179/2051645215Y.0000000002

[8] V. H. Tran, S. Lim, M. J. Park, D. S. Han, S. Phuntsho, H. Park, H. Matsuyama, H. K. Shon, Fouling and Performance of Outer Selective Hollow Fiber Membrane in Osmotic Membrane Bioreactor: Cross Flow and Air Scouring Effects, Bioresource Technology 295 (2020) 122303. doi:10.1016/j.biortech.2019.122303.
URL https://doi.org/10.1016/j.biortech.2019.122303

[9] P. K. Kang, W. Lee, S. Lee, A. S. Kim, Origin of structural parameter inconsistency in forward osmosis models: a pore-scale CFD study, Desalination 421 (2017) 47–60. doi:10.1016/j.desal.2017.05.018.
URL https://doi.org/10.1016/j.desal.2017.05.018

[10] Z. Cui, H. Hao Ngo, Z. Cheng, H. Zhang, W. Guo, X. Meng, H. Jia, J. Wang, Hysteresis effect on backwashing process in a submerged hollow fiber membrane bioreactor (MBR) applied to membrane fouling mitigation, Bioresource Technology 300 (2020) 122710. doi:10.1016/j.biortech.2019.122710.
URL https://doi.org/10.1016/j.biortech.2019.122710https://linkinghub.elsevier.com/retrieve/pii/S096085241931939X

[11] Y. Shimizu, Y.-I. Okuno, K. Uryu, S. Ohtsubo, A. Watanabe, Filtration Characteristics of Hollow Fiber Microfiltration Membranes Used in Membrane Bioreactor for Domestic Wastewater Treatment, Water Research 30 (10) (1996) 2385–2392. doi:

10.1016/0043-1354(96)00153-4.
URL https://doi.org/10.1016/0043-1354(96)00153-4

[12] S. Hong, T. Bae, T. Tak, A. Randall, Fouling control in activated sludge submerged hollow fiber membrane bioreactors, Desalination 143 (3) (2002) 219–228. doi:10.1016/S0011-9164(02)00260-6.

[13] I. Kim, D.-C. Choi, J. Lee, H.-R. Chae, J. Hee Jang, C.-H. Lee, P.-K. Park, Y.-J. Won, Preparation and application of patterned hollow-fiber membranes to membrane bioreactor for wastewater treatment, Journal of Membrane Science 490 (2015) 190–196. doi:10.1016/j.memsci.2015.04.026.
URL https://doi.org/10.1016/j.memsci.2015.04.026https://linkinghub.elsevier.com/retrieve/pii/S0376738815003579

[14] W. Rongwong, K. Goh, T.-H. Bae, Energy analysis and optimization of hollow fiber membrane contactors for recovery of dissolve methane from anaerobic membrane bioreactor effluent, Journal of Membrane Science 554 (2018) 184–194. doi:10.1016/j.memsci.2018.03.002.
URL https://doi.org/10.1016/j.memsci.2018.03.002https://linkinghub.elsevier.com/retrieve/pii/S0376738817327023

[15] G. Sethunga, W. Rongwong, R. Wang, T.-H. Bae, Optimization of hydrophobic modification parameters of microporous polyvinylidene fluoride hollow-fiber membrane for biogas recovery from anaerobic membrane bioreactor effluent, Journal of Membrane Science 548 (2018) 510–518. doi:10.1016/j.memsci.2017.11.059.
URL https://doi.org/10.1016/j.memsci.2017.11.059https://linkinghub.elsevier.com/retrieve/pii/S0376738817328715

[16] X. Liu, Y. Wang, T. D. Waite, G. Leslie, Numerical Simulations of Impact of Membrane Module Design Variables on Aeration Patterns in Membrane Bioreactors, Journal of

Membrane Science 520 (2016) 201–213. doi:10.1016/j.memsci.2016.07.011.
URL https://doi.org/10.1016/j.memsci.2016.07.011

[17] A. Berth, D. Lecouturier, K. Loubiere, P. Dhulster, G. Delaplace, Modelling and optimisation of gas-liquid mass transfer in a microporous hollow fiber membrane aerated bioreactor used to produce surfactin, Biochemical Engineering Journal 145 (2019) 109–119. doi:10.1016/j.bej.2018.10.029.
URL https://doi.org/10.1016/j.bej.2018.10.029https://linkinghub.elsevier.com/retrieve/pii/S1369703X18303930

[18] Y. Wang, J. Wang, H. Zhang, Y. Wu, A. Dang, Numerical and Experimental Investigation To Determine the Optimal Configuration of an Aeration Component in the Hollow Fiber Membrane Cleaning Process, RSC Advances 6 (26) (2016) 21600–21611. doi:10.1039/c5ra24544c.
URL https://doi.org/10.1039/c5ra24544c

[19] X. Guo, Y. Wang, H. Zhang, P. Li, C. Ma, Numerical and Experimental Investigation for Cleaning Process of Submerged Outside-In Hollow Fiber Membrane, Water Science and Technology 76 (6) (2017) 1283–1299. doi:10.2166/wst.2017.228.
URL https://doi.org/10.2166/wst.2017.228

[20] M. Wilkinson, On the Convergence of Soft Potential Dynamics To Hard Sphere Dynamics, Asymptotic Analysis 107 (1-2) (2018) 1–32. doi:10.3233/ASY-171448.
URL http://doi.org/10.3233/ASY-171448

[21] M. E. Rosti, A. A. Banaei, L. Brandt, A. Mazzino, Flexible Fiber Reveals the Two-Point Statistical Properties of Turbulence, Physical Review Letters 121 (4) (2018) 044501. doi:10.1103/PhysRevLett.121.044501.
URL https://doi.org/10.1103/physrevlett.121.044501https://link.aps.org/doi/10.1103/PhysRevLett.121.044501

[22] N. Sato, S. Makino, Numerical Analysis of the Motion of a Single Fiber Interacting With a Solid Wall in a Wall-Bounded Shear Flow, Journal of Non-Newtonian Fluid Mechanics 267 (2019) 51–60. doi:10.1016/j.jnnfm.2019.03.008.
URL https://doi.org/10.1016/j.jnnfm.2019.03.008

[23] A. S. Kim, Constraint Dissipative Hydrodynamics (HydroRattle) Algorithm for Aggregate Dynamics, Chemistry Letters 41 (10) (2012) 1285–1287. doi:10.1246/cl.2012.1285.
URL http://www.journal.csj.jp/doi/10.1246/cl.2012.1285

[24] J.-P. Ryckaert, G. Ciccotti, H. J. Berendsen, Numerical integration of the cartesian equations of motion of a system with constraints: molecular dynamics of n-alkanes, Journal of Computational Physics 23 (3) (1977) 327–341. doi:10.1016/0021-9991(77)90098-5.
URL https://linkinghub.elsevier.com/retrieve/pii/0021999177900985

[25] H. C. Andersen, Rattle: A {"Velocity"} version of the shake algorithm for molecular dynamics calculations, Journal of Computational Physics 52 (1) (1983) 24–34. doi:10.1016/0021-9991(83)90014-1.
URL https://linkinghub.elsevier.com/retrieve/pii/0021999183900141

[26] A. S. Kim, Y. Liu, Irreversible Chemical Potential and Shear-Induced Diffusion in Cross-flow Filtration, Industrial & Engineering Chemistry Research 47 (15) (2008) 5611–5614. doi:10.1021/ie0714403.
URL https://pubs.acs.org/doi/10.1021/ie0714403

[27] L. Durlofsky, J. F. Brady, G. Bossis, Dynamic simulation of hydrodynamically interacting particles, Journal of Fluid Mechanics 180 (-1) (1987) 21. doi:10.1017/S002211208700171X.
URL http://www.journals.cambridge.org/abstract{_}S002211208700171X

[28] S. Kim, S. J. Karrila, Microhydrodynamics: Principles and Selected Applications, Butterworth-Heinemann, 2013.

[29] M. R. Maxey, Equation of motion for a small rigid sphere in a nonuniform flow, Physics of Fluids 26 (4) (1983) 883. doi:10.1063/1.864230.
URL https://aip.scitation.org/doi/10.1063/1.864230

[30] A. B. Basset, Treatise on Hydrodynamics, Vol. 2, Dover Publications, New York, NY, 1888.

[31] J. C. Chen, A. S. Kim, Monte Carlo simulation of colloidal membrane filtration: Principal issues for modeling, Advances in Colloid and Interface Science 119 (1) (2006) 35–53. doi:10.1016/j.cis.2005.09.006.
URL https://linkinghub.elsevier.com/retrieve/pii/S0001868605001119

[32] J. CHEN, M. ELIMELECH, A. KIM, Monte carlo simulation of colloidal membrane filtration: Model development with application to characterization of colloid phase transition, Journal of Membrane Science 255 (1-2) (2005) 291–305, chen-2005-monte-carlo-simul.pdf. doi:10.1016/j.memsci.2005.02.004.
URL https://doi.org/10.1016/j.memsci.2005.02.004

	Variables	Value	Value
Rack	Fiber length [mm], L_f	1000	2000
	Number of spheres, N_p	500	1000
	Stack height [mm], $H = L_f/(1 + R_{st})$	998	1996
	Oscillation Amplitude [mm], A	60.0	120.0
	Oscillation frequency [Hz], ω	0.46	0.46

Table 1: Simulation parameters of the rack and fibers, where the oscillation amplitude is calculated as $A = 0.06\,L_f$ and the stack ratio of $R_{\mathrm{st}} = 0.2\,\%$ is used. Based on the common frequency, the period of the rack oscillation is calculated as $\tau = 2.1739$ s.

	Variables	PVDF	PET
Fiber	Solid density, ρ_s	1.780	1.380
	Outer diameter [mm], $d_o = 2a_f$	2.000	2.000
	Inner diameter [mm], $d_i = 2a'_f$	1.600	0.700
	Thickness [mm], $a_f - a_{\prime f}$	0.200	0.650
	Porosity [-], ϵ	0.650	0.650
	Water-filled fiber material density, $\bar{\rho}_f$	1.273	1.133
	Mass of cylindrical segment [mg], m_s	6.901	7.017
Sphere	Volume [mm^3]	4.189	4.189
	Specific gravity [–], s_g	1.647	1.675

Table 2: Simulation parameters of the and fibers and equivalent spheres, made of polyvinylidene fluoride (PVDF) and polyethylene terephthalate (PET).

	1 m PVDF		2 m PVDF	
	x-dir.	z-dir.	x-dir.	z-dir.
$\boldsymbol{f}_f$ or $\boldsymbol{f}_b$ [μN]	$O\left(10^0\right)$	$O\left(10^1\right)$	$O\left(10^1\right)$	$O\left(10^2\right)$
$\boldsymbol{f}_s$ [μN]	$O\left(10^{-1}\right)$	$O\left(10^{-1}\right)$	$O\left(10^0\right)$	$O\left(10^0\right)$
resultant $\boldsymbol{F}$ [μN]	$O\left(10^{-2}\right)$	$O\left(10^{-2}\right)$	$O\left(10^{-1}\right)$	$O\left(10^{-1}\right)$
Fig. No.	(7)	(8)	(10)	(11)

Table 3: Analysis of force magnitudes, exerted on 1 m and 2 m PVDF HF membranes in x- and z-directions.

Figure 1: The shaking HF bundle, attached to the ceiling and bottom of the rack surfaces to mitigate particulate fouling on the HF surfaces. (https://www.coepro.com/en/pages/water-plants).

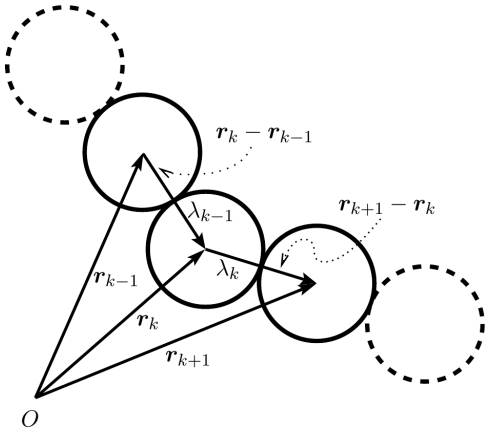

Figure 2: Schematic configuration of a chain as a connection of equal-sized spheres.

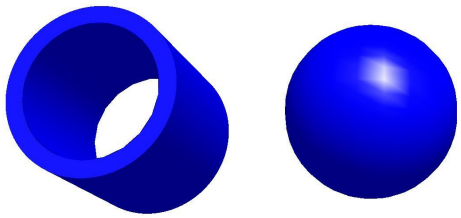

Figure 3: A hollow fiber and the equivalent sphere. The hollow cylinder has height $2a_f$, equal to diameters of the sphere and the outer cylindrical surface. The sphere has a uniformly distributed mass m_s equal to that of the hollow fiber of which lumen and porous spaces are filled with water.

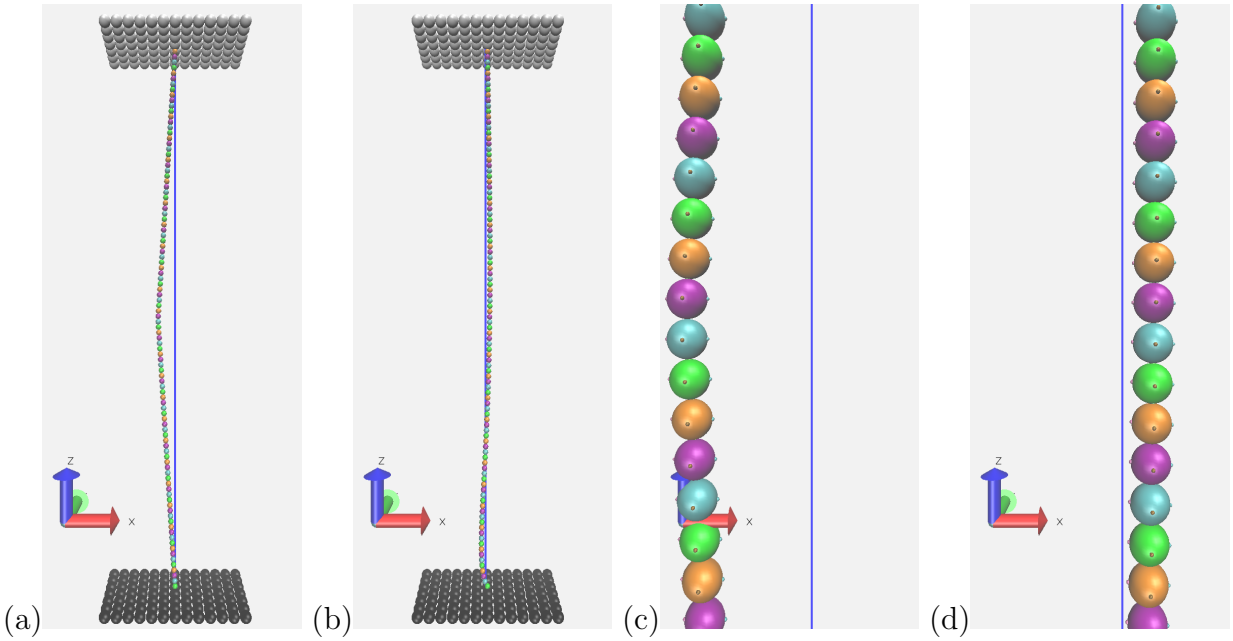

Figure 4: A short hollow fiber ($N_p = 100$) as a sphere-connected chain: overview at (a) $t = 0$ s and (b) $t = 0.0783$ s; and (c) and (d) show closer views of (a) and (b), respectively. The length of this short fiber is $l_f = N_p \times (2a_f) = 200\,\text{mm}$ and the blue vertical line connect two points of $(0, 0, -a_p)$ and $(0, 0, H - a_p)$.

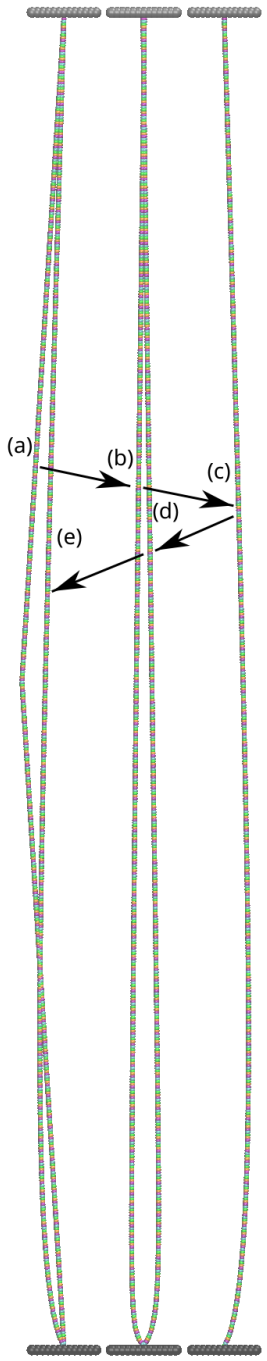

Figure 5: Snapshot of a moving chain, i.e., a PVDF hollow fiber membrane immediately after time (a) 0, (b) 0.25τ, (c) 0.5τ, (d) 0.75τ, and (e) 1.0τ. The rack location, i.e., position s of the top and bottom plates, are equal at time $t = 0$ and τ and time $t = 0.25\tau$ and 0.75τ. The configuration of (a) and (b) on the left-hand sides of (e) and (d), respectively. For a better visualization, sphere diameters are enlarged 1.5 times.

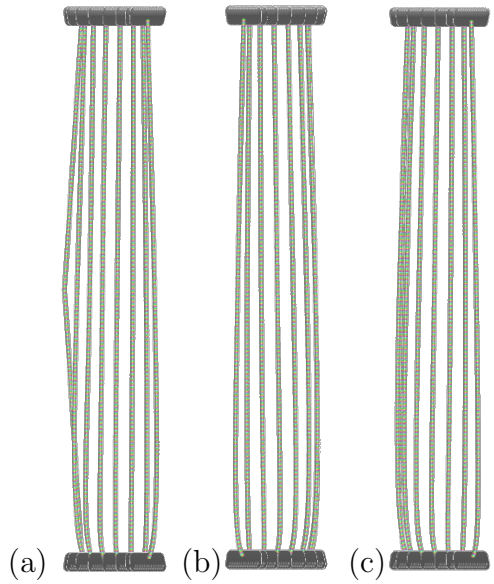

Figure 6: Reciprocation snapshots of 1 m PVDF hollow fiber during (a) $0 \leq t \leq 0.5\tau$ (initially moving to the right), (b) $0.5\tau \leq t \leq \tau$ (returned and moving to the left), and (c) $\tau \leq t \leq 1.5\tau$ (after one full reciprocation, moving to the right again). For visualization, the sphere diameters are enlarged four times.

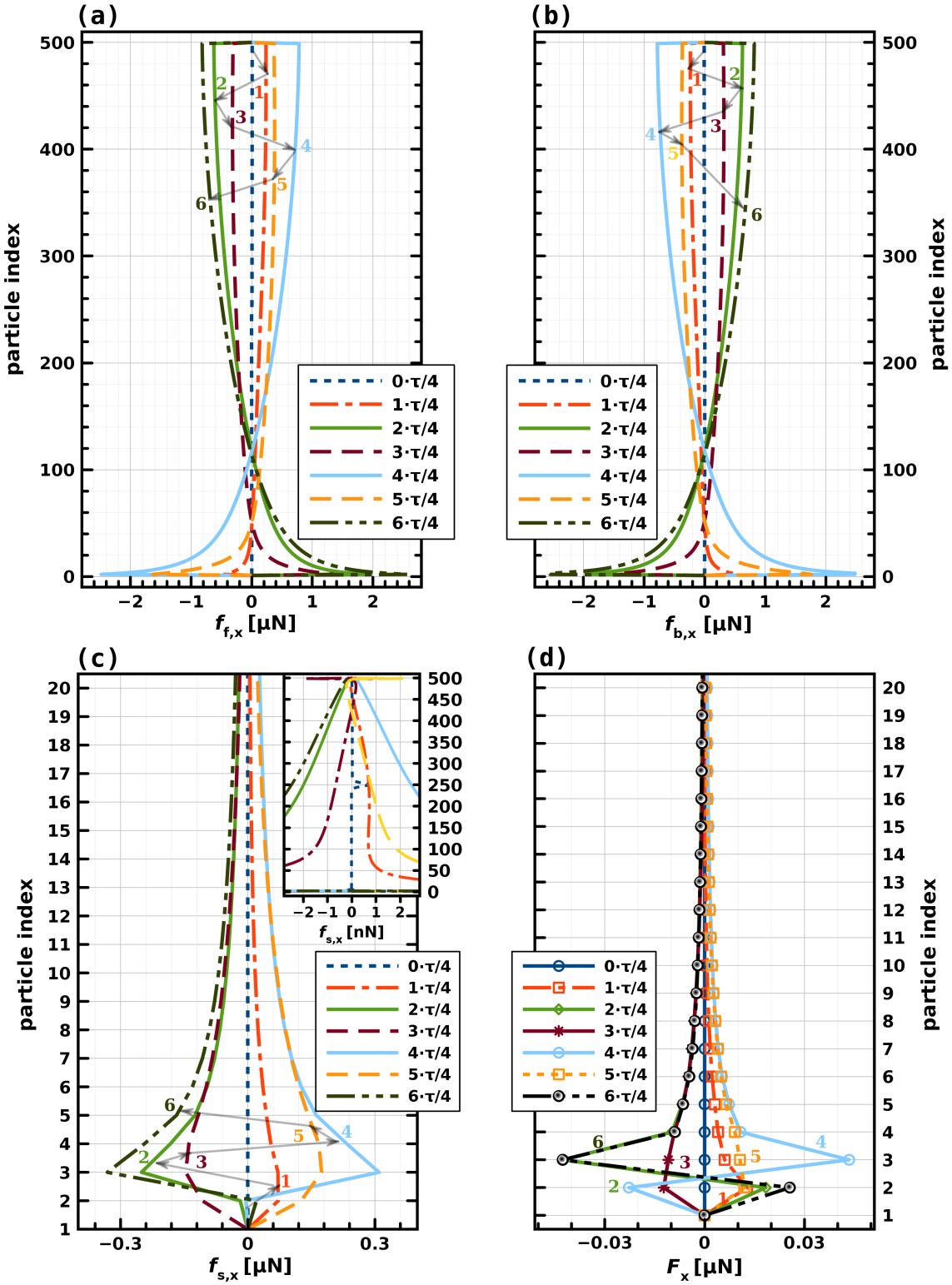

Figure 7: The $x-$directional forces exerted on the 1 m PVDF hollow fiber: (a) forward constraint, (b) backward constraint, (c) net constraint and (d) net resultant.

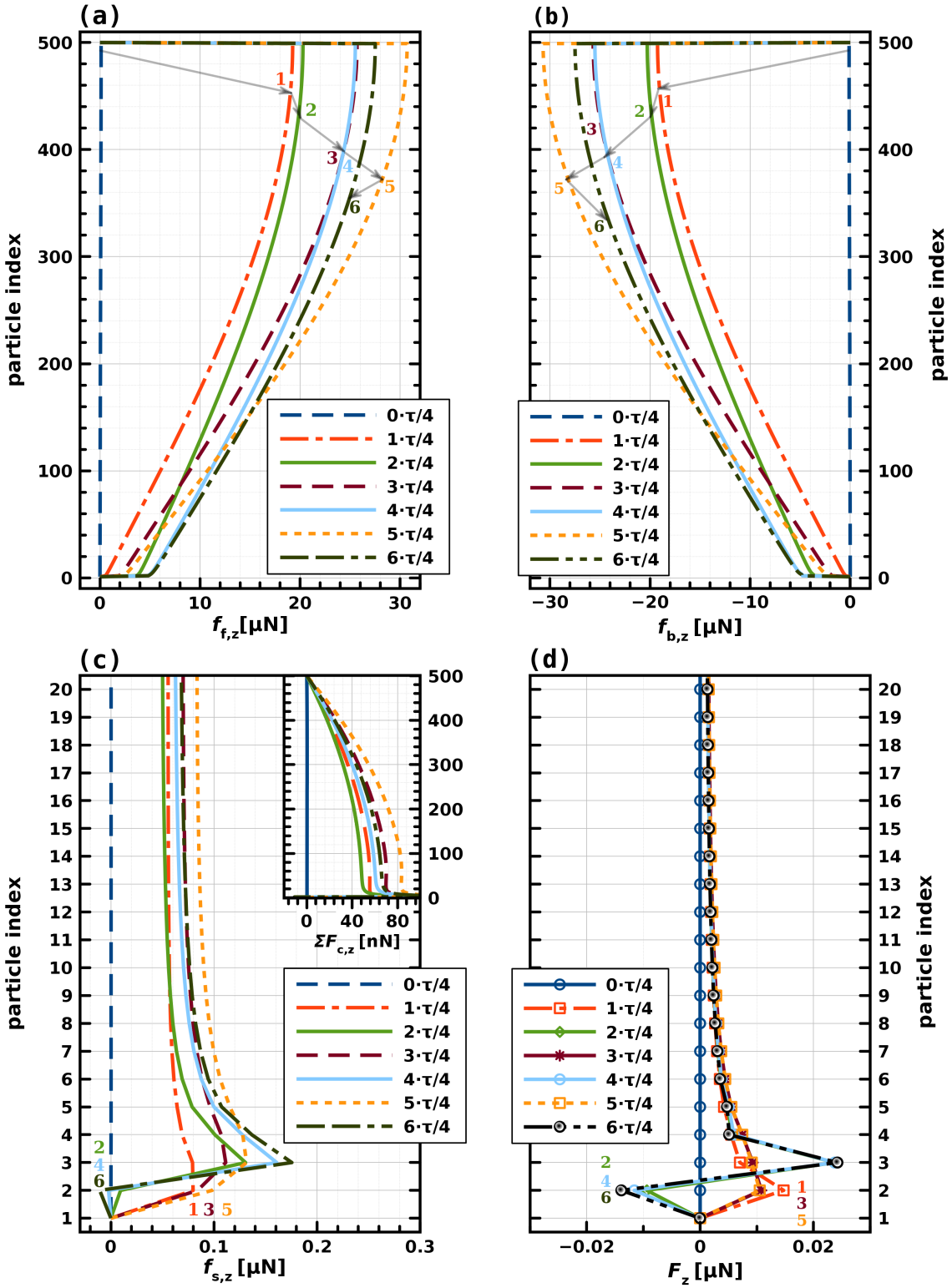

Figure 8: The $z-$directional forces exerted on the 1 m PVDF hollow fiber: (a) forward constraint, (b) backward constraint, (c) net constraint and (d) net resultant.

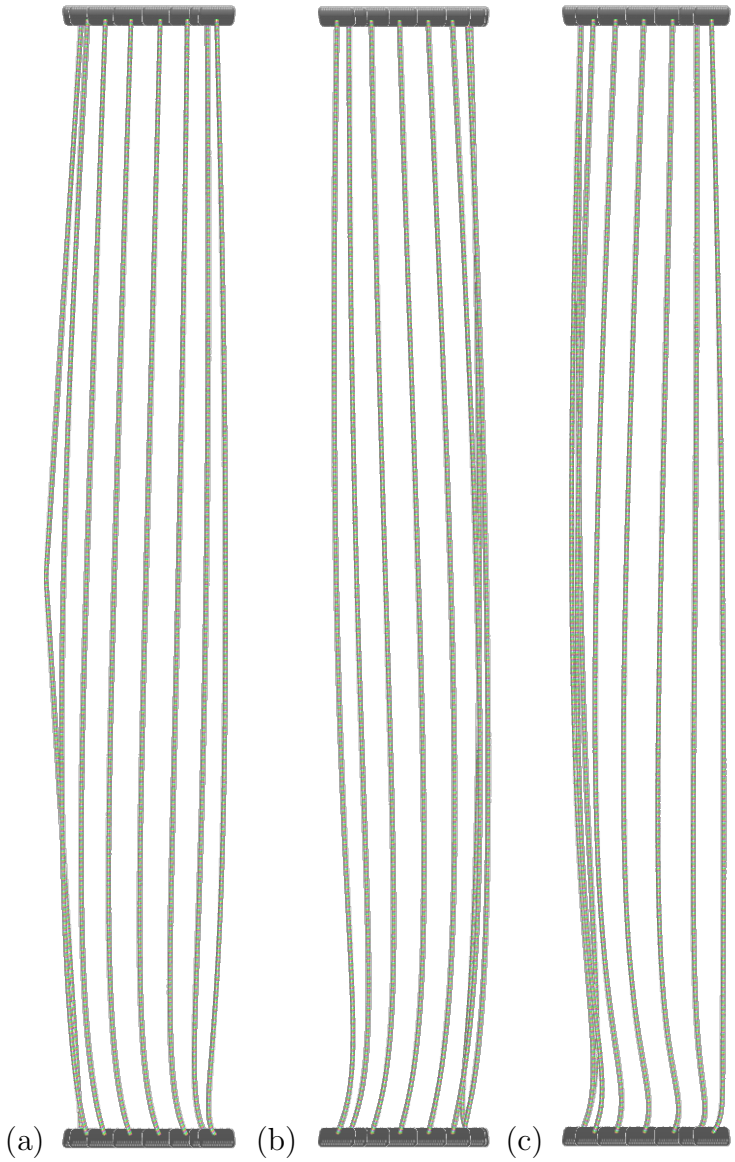

Figure 9: Reciprocation snapshots of 2 m PVDF hollow fiber during (a) $0 \leq t \leq 0.5\tau$ (initially moving to the right), (b) $0.5\tau \leq t \leq \tau$ (returned and moving to the left), and (c) $\tau \leq t \leq 1.5\tau$ (after one full reciprocation, moving to the right again). For visualization, the sphere diameters are enlarged four times.

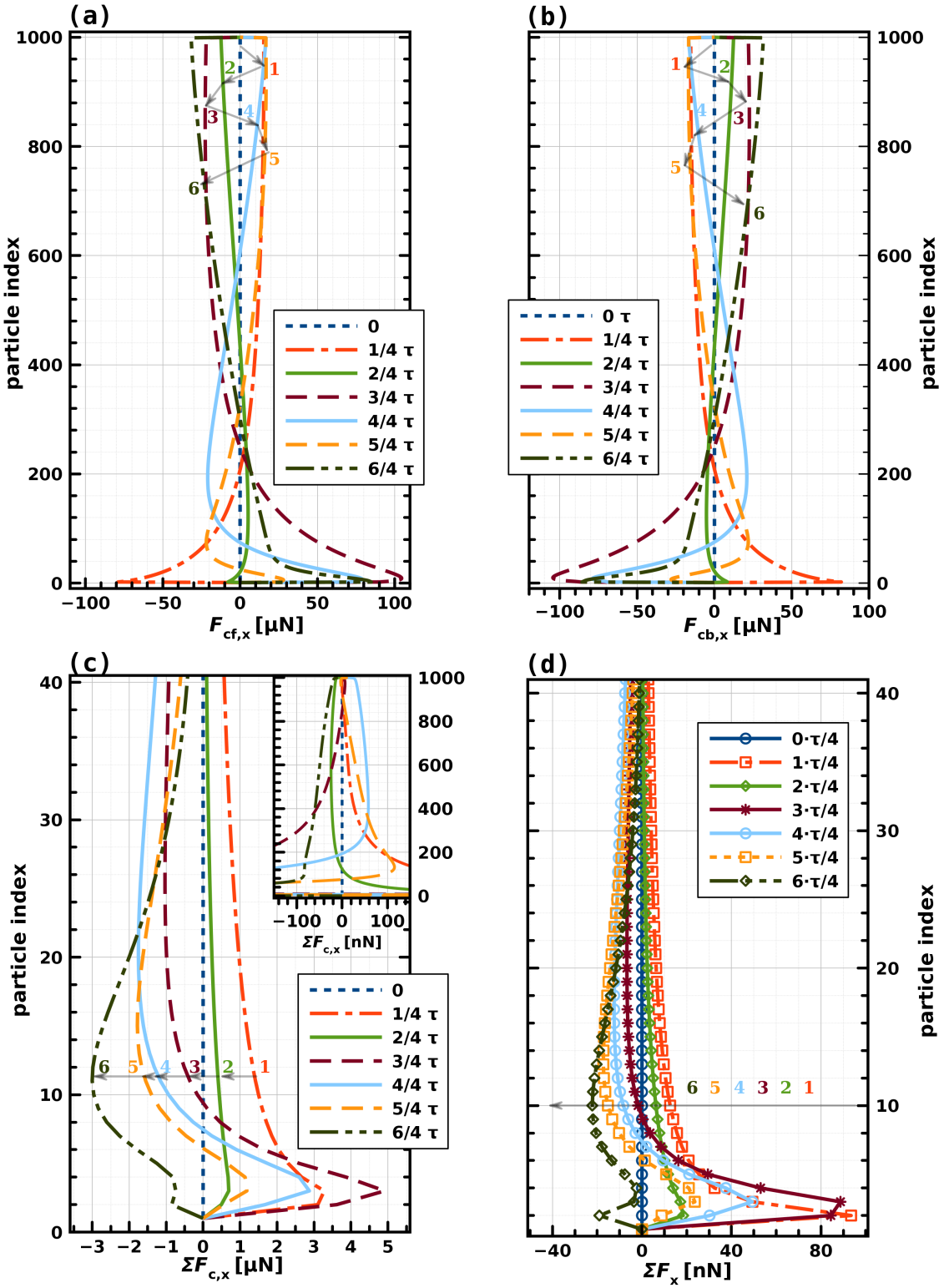

Figure 10: The $x-$directional forces exerted on the 2 m PVDF hollow fiber: (a) forward constraint, (b) backward constraint, (c) net constraint and (d) net resultant.

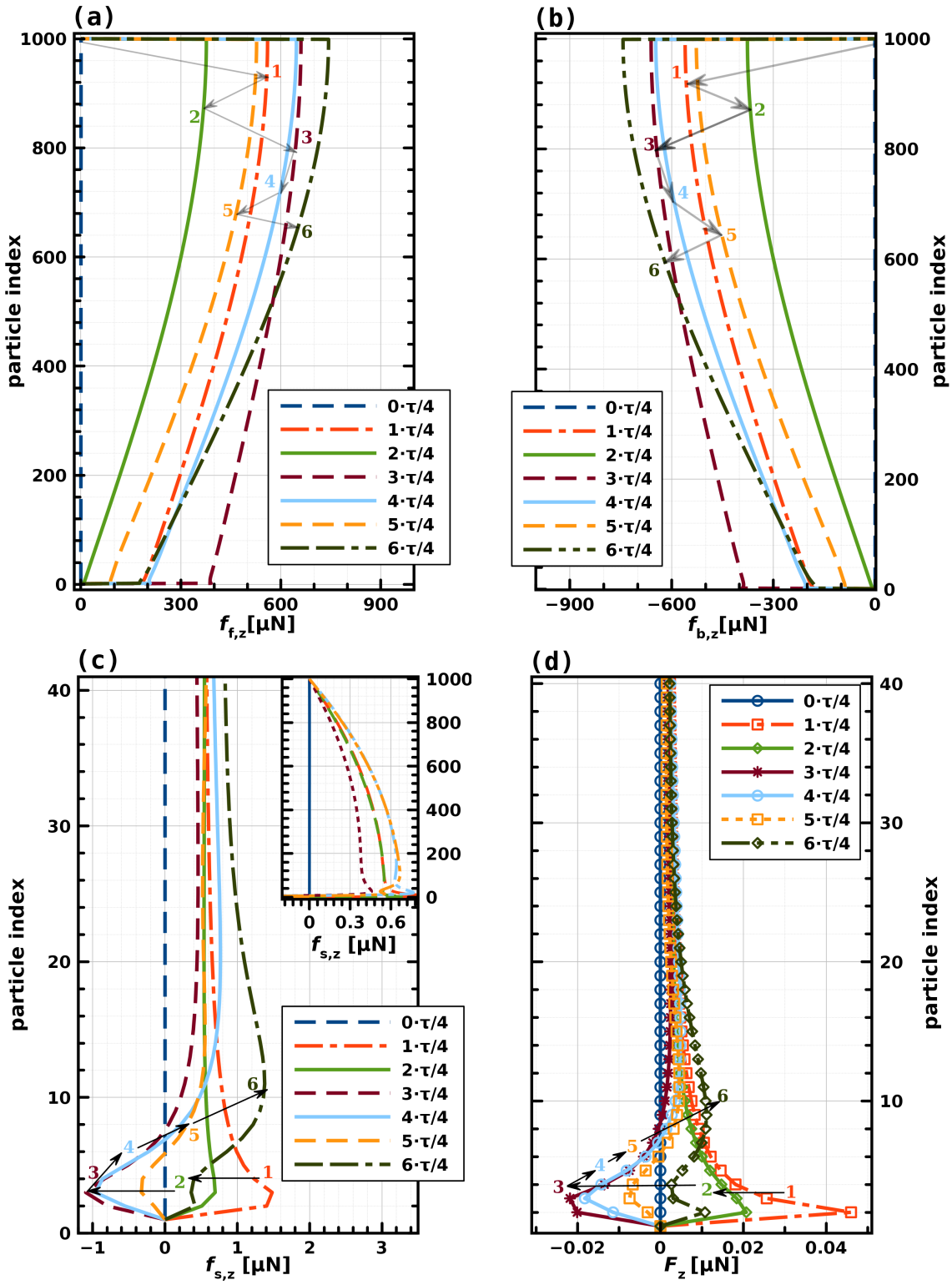

Figure 11: The $z-$directional forces exerted on the 2 m PVDF hollow fiber: (a) forward constraint, (b) backward constraint, (c) net constraint and (d) net resultant.

Appendix. Simulation results of 1 m and 2 m PET Hollow fiber membranes

Figs. A.1 and A.2 show the force profiles of the 1 m PET HF membrane in the x- and z-directions, respectively, which appear similar to those of the 1 m PVDF HF membrane, as shown in Figs. 7 and 8, respectively. Figs. A.3 and A.4 show the force profiles of the 2 m PET HF membrane in x- and z-directions, respectively, which appear similar to those of the 2 m PVDF HF membrane, as shown in Figs. 10 and 11, respectively. Due to the small difference in specific gravity values of equal-sized PVDF and PET spheres, i.e., 1.647 and 1.675, overall trends of the specific profiles of forces exerted on the PET HF membrane are similar to those on the PVDF HF membrane both qualitatively and quantitatively.

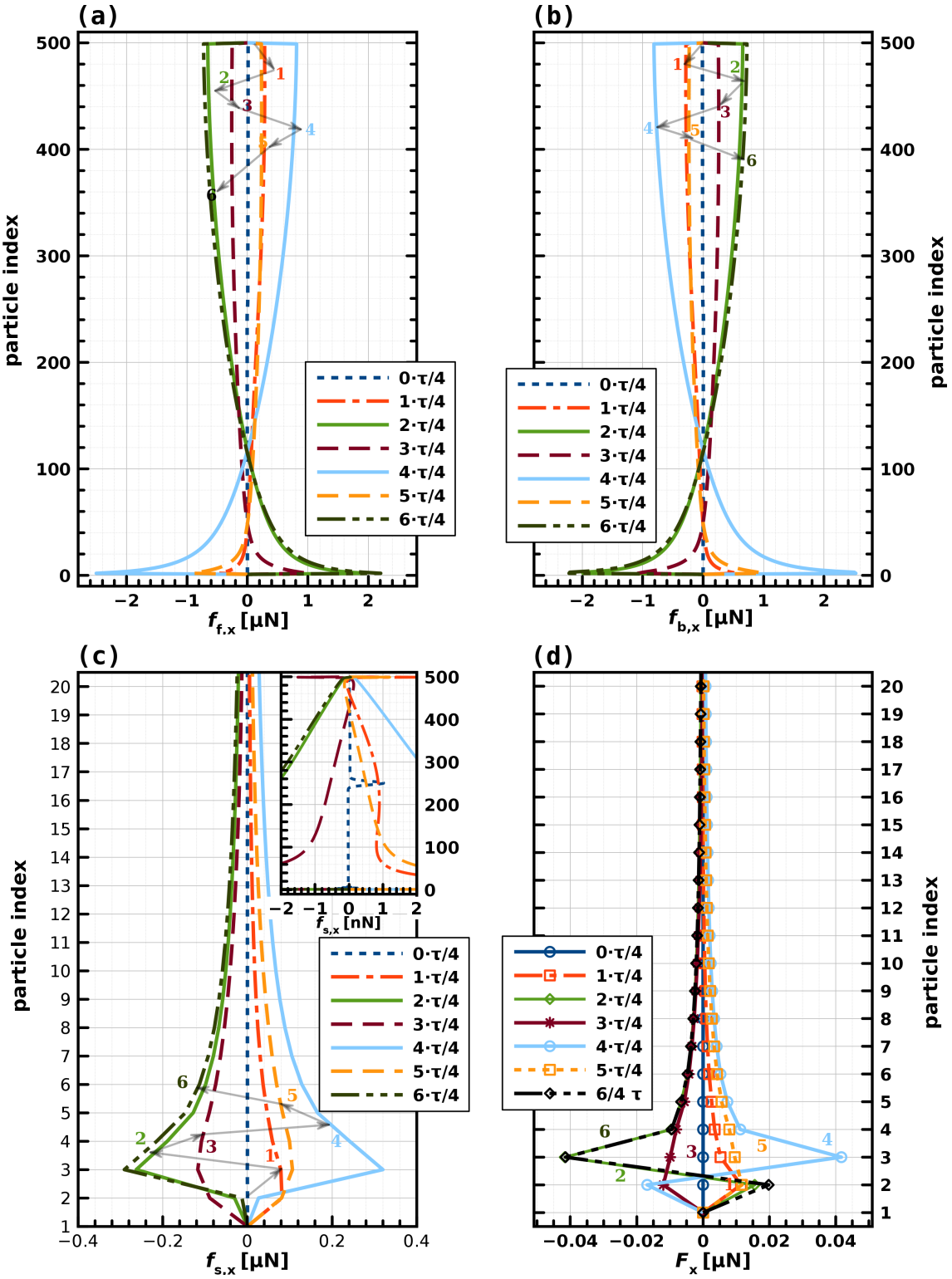

Figure A.1: The $x-$directional forces exerted on the 1 m PET hollow fiber: (a) forward constraint, (b) backward constraint, (c) net constraint, and (d) net resultant.

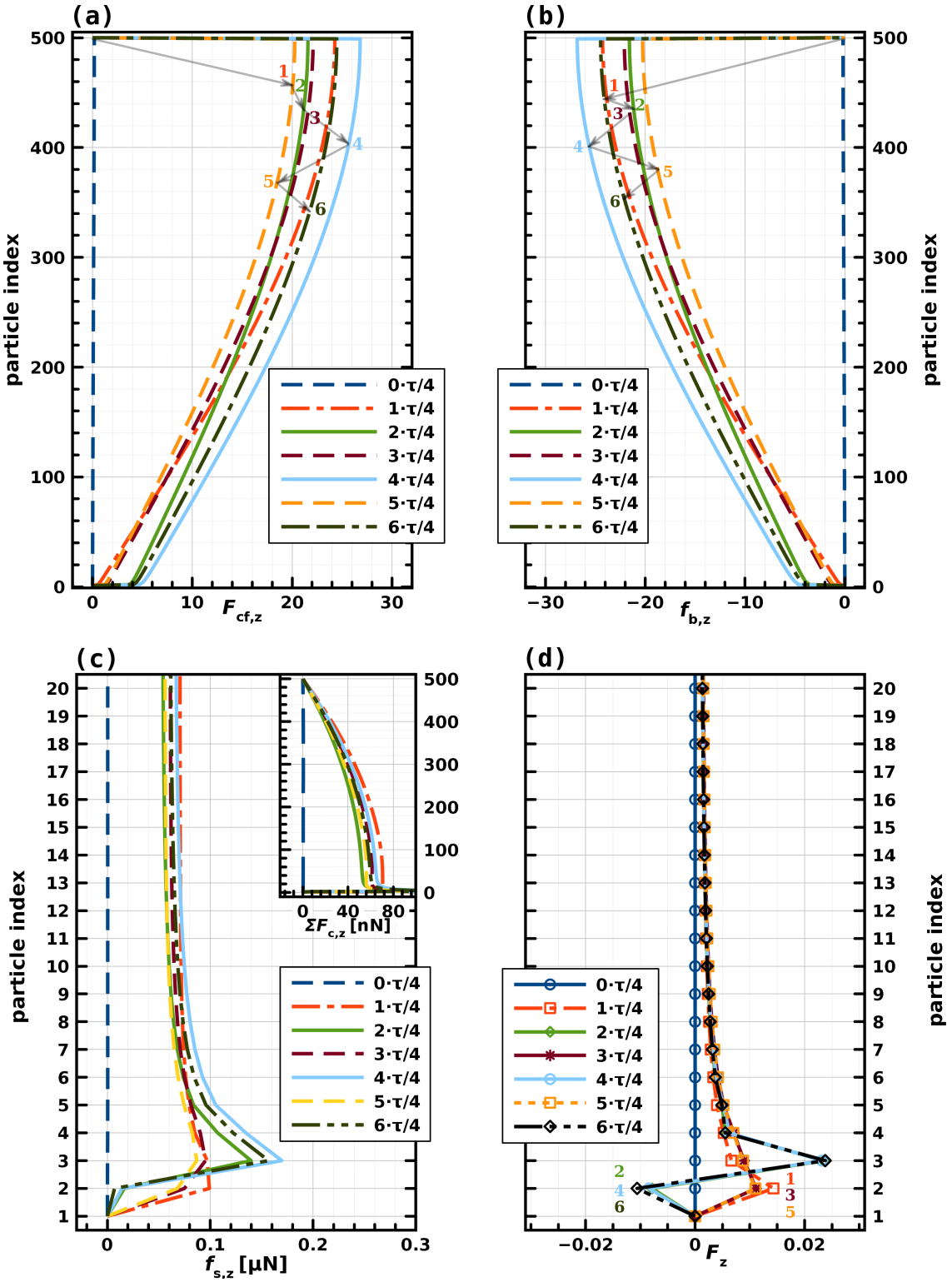

Figure A.2: The $z-$directional forces exerted on the 1 m PET hollow fiber: (a) forward constraint, (b) backward constraint, (c) net constraint, and (d) net resultant.

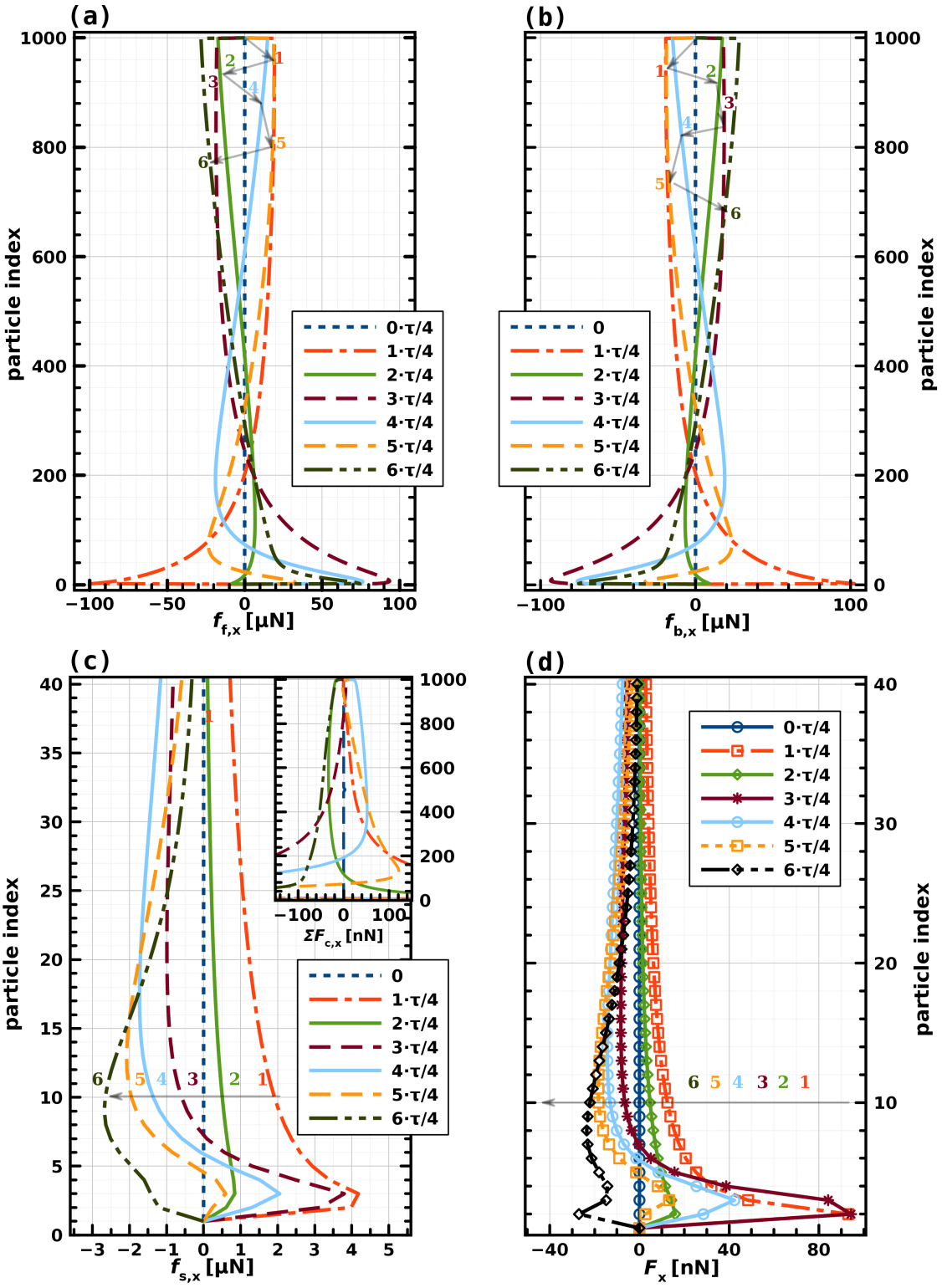

Figure A.3: The $x-$directional forces exerted on the 2 m PET hollow fiber: (a) forward constraint, (b) backward constraint, (c) net constraint, and (d) net resultant.

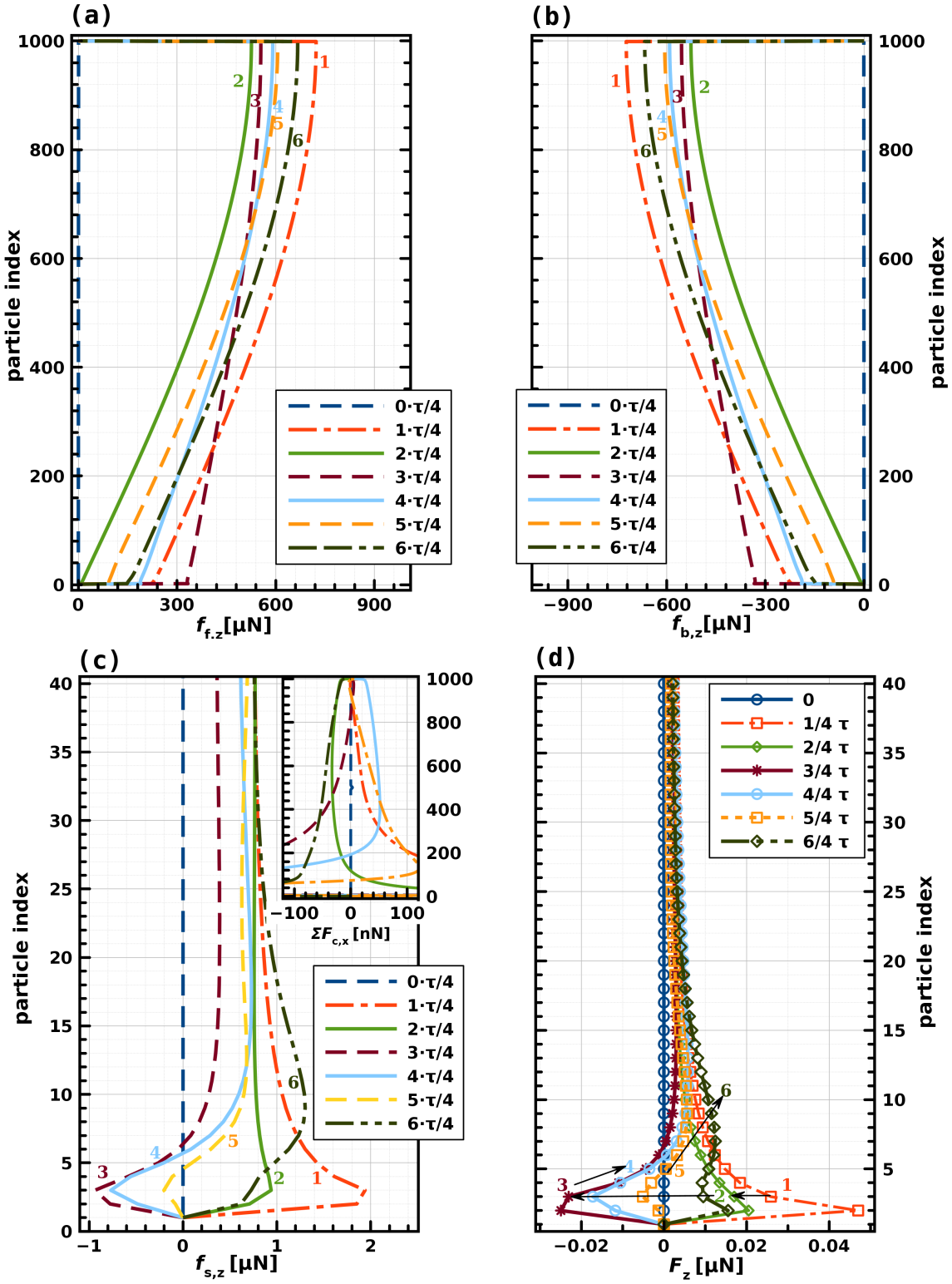

Figure A.4: The $z-$directional forces exerted on the 2 m PET hollow fiber: (a) forward constraint, (b) backward constraint, (c) net constraint, and (d) net resultant.